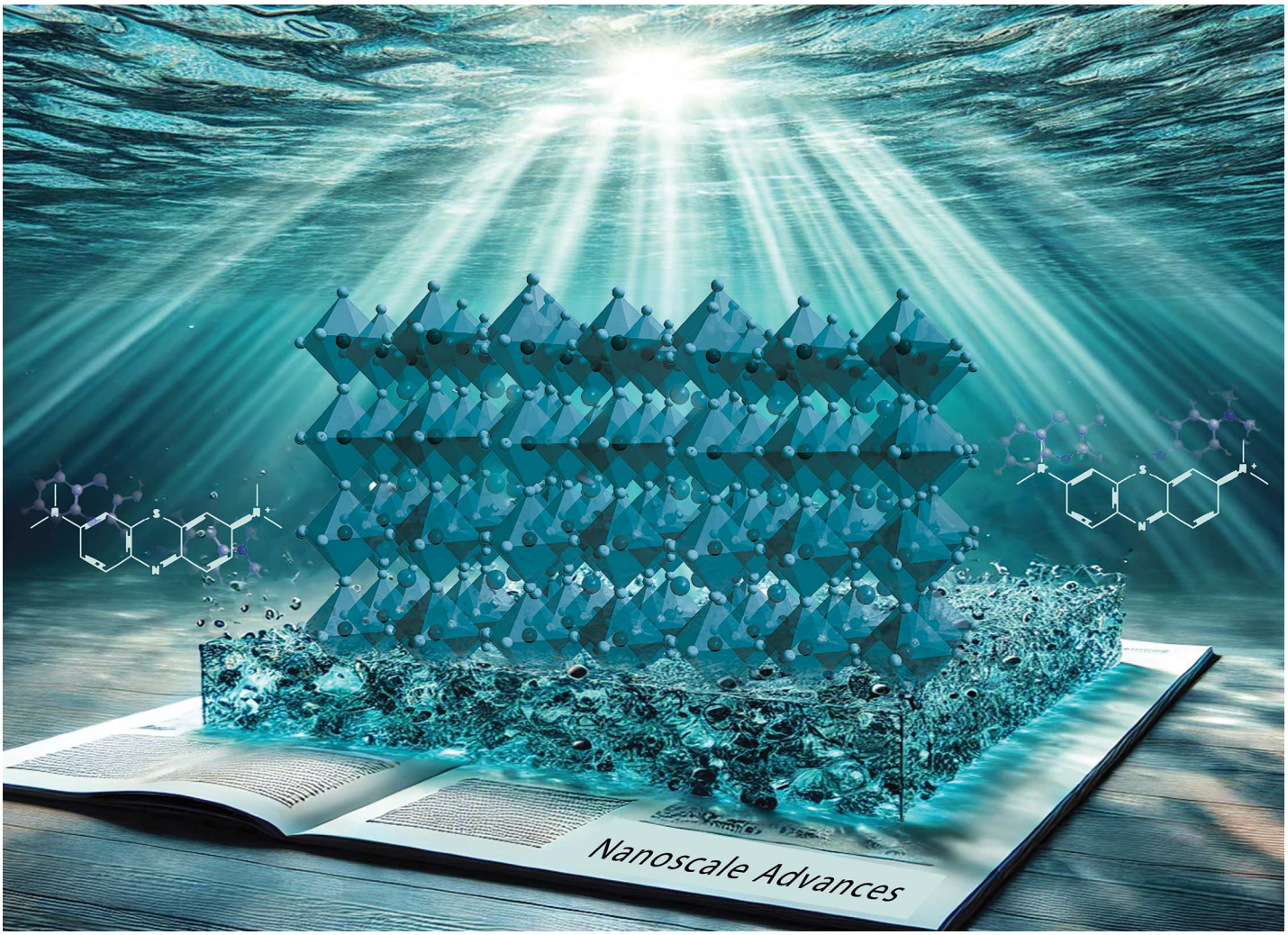

Showcasing research from Mohamed Masri, Girisha. K. B, Abdo Hezam, Khaled Alkanad, Talal F. Qahtan, Qasem A. Drmosh, Kalappa Prashantha, Manjunath S. H, Sanaa Mohammed Abdu Kaid, K. Byrappa, and Faten Masri, Department of Mechanical Engineering, BGS Institute of Technology, Adichunchanagiri University, B. G. Nagar, Karnataka, India.

Synergetic efficiency: *in situ* growth of a novel 2D/2D chemically bonded $Bi_2O_3/Cs_3Bi_2Br_9$ S-scheme heterostructure for improved photocatalytic performance and stability

An innovative solution for the instability problem of catalysts in aqueous media was offered *via* synthesizing stable 2D $Bi_2O_3/Cs_3Bi_2Br_9$ nanosheets by optimizing the mixing ratio between Bi_2O_3 and $Cs_3Bi_2Br_9$. Bi co-sharing has enhanced the S-scheme charge carrier leading to the improvement of photocatalytic degradation of methylene blue.

As featured in:

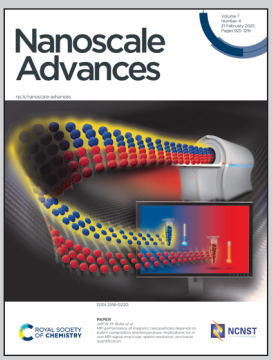

See Faten Masri *et al.*, *Nanoscale Adv.*, 2025, **7**, 1030.

ROYAL SOCIETY OF CHEMISTRY

rsc.li/nanoscale-advances

Registered charity number: 207890

Nanoscale Advances

ROYAL SOCIETY OF CHEMISTRY

PAPER

View Article Online
View Journal | View Issue

Cite this: *Nanoscale Adv.*, 2025, **7**, 1030

Synergetic efficiency: *in situ* growth of a novel 2D/2D chemically bonded $Bi_2O_3/Cs_3Bi_2Br_9$ S-scheme heterostructure for improved photocatalytic performance and stability†

Mohamed Masri,[ab] Girisha K. B.,[b] Abdo Hezam,[cd] Khaled Alkanad,[e] Talal F. Qahtan,[f] Qasem A. Drmosh,[gh] Kalappa Prashantha,[a] Manjunath S. H.,[b] Sanaa Mohammed Abdu Kaid,[a] K. Byrappa[a] and Faten Masri*[i]

Adverse reactions caused by waterborne contaminants constitute a major hazard to the environment. Controlling the pollutants released into aquatic systems through water degradation has been one of the major concerns of recent research. Bismuth-based perovskites have exhibited outstanding properties in the field of photocatalysis. Nonetheless, many proposed bismuth-based perovskites still suffer from stability problems. The present study investigated a unique bismuth-based metal-co-sharing composite of 2D $Bi_2O_3/Cs_3Bi_2Br_9$ nanosheet perovskite synthesized *via* a modified anti-solvent reprecipitation method. Several samples were prepared using different ratios of Bi_2O_3 and $Cs_3Bi_2Br_9$. The optimal composite sample was found to be BO/CBB 28%, where 2D stacked nanosheets of $Cs_3Bi_2Br_9$ showed remarkable interaction with Bi_2O_3 due to its optimal Bi co-sharing, as displayed in the FE-SEM and HRTEM images. However, further increasing the percentage led to greater agglomeration, hindering the photocatalytic degradation efficiency. The average size and optical band gap energy of the optimal sample were 42.5 nm and 2.46 eV, respectively. The photocatalytic degradation of MB using the optimal sample reached ~92% within 60 min with a catalyst dosage of 10 mg L^{-1}. With an increase in catalyst concentration to 40 mg L^{-1}, MB removal reached almost ~96% within 60 min under visible light owing to the enhanced stability, facilitating efficient charge separation. This paper presents an improved composite with optimal ratios of 2D $Bi_2O_3/Cs_3Bi_2Br_9$ nanosheets that demonstrated good stability and enhanced photocatalytic performance in comparison with pure Bi_2O_3 and $Cs_3Bi_2Br_9$. This study also sheds light on the significance of metal co-sharing and the pivotal role it plays in enhancing the S-scheme charge transfer and the internal electric field between the two components.

Received 18th December 2024
Accepted 29th December 2024

DOI: 10.1039/d4na01047g

rsc.li/nanoscale-advances

1. Introduction

The rapid increase in the world population, the expansion of urbanization, and the issue of climate change have led the world into a water and energy crisis. Water and energy consumption are intensifying; however, their resources are limited, leading to a severe shortage of these two important factors for life on Earth.[1,2] Addressing the water and energy predicament has been imperative for researchers, resulting in the investigation of several water- and energy-preservation methods. To maintain the sustainability of these two vital resources, researchers have devoted significant effort towards adopting solar energy and water-treatment practices.[3–8] Conventionally, wastewater contaminant degradation can be achieved through the utilization of physical, biological, or chemical methods.[9–12] Photocatalysis is one of the most promising techniques for wastewater degradation due to its environmentally friendly qualities, durability, low cost, and

[a]*Center for Research and Innovations, BGS Institute of Technology, Adichunchanagiri University, B. G. Nagar, Karnataka, India*
[b]*Department of Mechanical Engineering, BGS Institute of Technology, Adichunchanagiri University, B. G. Nagar, Karnataka, India*
[c]*Leibniz-Institute for Catalysis, University of Rostock, 18059 Rostock, Germany*
[d]*Industrial Chemistry and Heterogeneous Catalysis, Department of Chemistry, TUM School of Natural Sciences, Technical University of Munich, 85748 Garching, Germany*
[e]*Department of Studies in Physics, University of Mysore, Manasagangotri, Mysuru, Karnataka, India*
[f]*Physics Department, College of Science and Humanities in Al-Kharj, Prince Sattam Bin Abdulaziz University, Al-kharj 11942, Saudi Arabia*
[g]*Interdisciplinary Research Centre for Hydrogen Technologies and Carbon Management, King Fahd University of Petroleum and Minerals (KFUPM), Dhahran, 31261, Saudi Arabia*
[h]*Department of Materials Science and Engineering, King Fahd University of Petroleum and Minerals (KFUPM), Dhahran, 31261, Saudi Arabia*
[i]*Department of Production Engineering, Faculty of Mechanical Engineering, University of Aleppo, Aleppo, Syria. E-mail: faten.masri.or@gmail.com*

† Electronic supplementary information (ESI) available. See DOI: https://doi.org/10.1039/d4na01047g

enhanced performance in destroying and removing contaminants.[13–16] In photocatalysis, chemical reactions are promoted under light energy using several materials, such as metal oxides, semiconductors, and organic compounds.[17]

The catalytic properties are pivotal for achieving photocatalytic reactions. As such, careful selection of the photocatalyst is crucial for effective performance. Perovskite materials have demonstrated remarkable optoelectrical properties, rendering them a promising option for harvesting light and executing photocatalytic reactions, including for water treatment.[18–20] Recently, several scholarly studies have proposed perovskites as promising semiconductors for photocatalytic reactions due to their unique characteristics, such as regulated redox cycles, strong conversion adaptability, long carrier diffusion lengths, notable tolerance factors, and high photocorrosion stability. The crystal structure of perovskites permits their bandgap to be adjusted to increase their visible light absorption, which means they can be tailored to suit the required reaction.[21] Furthermore, the lattice structure of perovskites can have a substantial impact on photogenerated charge-carrier separation.[22] The identified cubic shape of perovskites allows for the insertion of a wide range of metal ions.[23] Moreover, perovskites are cost-effective, flexible, and thermally resistant. Thus, all of the aforementioned properties suggest perovskites would be good candidates for photocatalytic applications.[24,25]

Initially, the perovskites employed as photocatalysts were based on lead, and they demonstrated enhanced photocatalytic activity compared to their traditional counterparts.[26] However, the commercialization of lead-based perovskites was hampered due to their solubility in water, resulting in a toxic release of lead into water. Alternative lead-free perovskites with similar ionic radii to Pb emerged as promising less-toxic, low-cost, and efficient candidates for photocatalytic applications.[27] Lead-free bismuth-based perovskites $Cs_3Bi_2X_9$ have been selected as catalysts by many researchers because of their excellent optical properties, moderate band gaps, and robustness under ambient conditions.[28–31] Besides, they exhibit excellent organic dye degradation capabilities. For instance, $Cs_3Bi_2I_9$ could effectively remove 93% of rhodamine B (RhB) in 180 min under visible light.[32] Similarly in another study, rhodamine 6G dye (RhG) was degraded using synthesized $Cs_3Bi_2Br_9$ as a photocatalyst, and the reported results revealed a remarkable photocatalytic activity of the synthesized photocatalyst.[33] Nonetheless, the susceptibility of $Cs_3Bi_2Br_9$ to degradation under humid conditions hinders its stability as water molecules could cause the decomposition of $Cs_3Bi_2Br_9$.

Recently, Masri *et al.* addressed the instability issue of $Cs_3Bi_2Br_9$ in aqueous environments through making use of the unique properties of two-dimensional (2D) perovskite nanosheets. They prepared 2D $Cs_3Bi_2Br_9$ perovskite nanosheets as photocatalysts for the removal of contaminants from water. Different scans of the prepared 2D $Cs_3Bi_2Br_9$ perovskite nanosheets showed they possessed abundant active sites for the adsorption and reaction with the target pollutants. Due to the high reactivity of the catalyst's surface, the contact between the catalyst and the water contaminants was enhanced, leading to the successful degradation of the contaminants in water.[20] In fact, the morphology, including the thickness and composition, of 2D perovskite nanosheets allows for the formation of flexible bandgaps that permit harnessing a broader spectrum of light energy, which can facilitate initiating and accelerating chemical reactions under a wide range of light irradiation,[20,34–37] whereby, 2D $Cs_3Bi_2Br_9$ perovskite nanosheets displayed improved photocatalytic performance for the removal of dyes.

Much research has investigated the degradation of several pollutant dyes *via* oxide-based photocatalysts, which have exhibited good degradation activities.[38] Oxide-based photocatalysts are considered excellent materials for the elimination of water contaminants due to their non-toxicity, cost-effectiveness, and durability together with exceptional optoelectrical properties. Over several decades, numerous nanometal oxides, including ZnO, Mn_2O_3, Fe_3O_4, TiO_2, and Fe_2O_3, have been used to degrade plenty of dye molecules.[39–42] Although each of the aforementioned materials has demonstrated a satisfactory degradation efficiency, major deficiencies have also been found, such as agglomeration, fast electron–hole recombination, and inefficient bandgap values.[43–45] Bi_2O_3 possesses many beneficial physiochemical properties, such as an appropriate bandgap, high refractive index, high metal oxide ion-conductivity properties, dielectric permittivity, superior photoconductivity, and photoluminescence properties, in addition to being an eco-friendly material.[46–48] Hence, many research studies have experimented with Bi_2O_3 for water degradation.[49]

In the present study, we developed an innovative solution to tackle the instability problem of catalysts in aqueous media by synthesizing stable 2D $Bi_2O_3/Cs_3Bi_2Br_9$ nanosheets. Through a modified anti-solvent reprecipitation method, we accomplished a remarkable achievement: the successful preparation of 2D $Bi_2O_3/Cs_3Bi_2Br_9$ nanosheets by optimizing the mixing ratio between Bi_2O_3 and $Cs_3Bi_2Br_9$. By leveraging the distinctive characteristics of both bismuth oxide and bismuth halide perovskites, and harnessing the benefits of the 2D structures in $Cs_3Bi_2Br_9$ and Bi_2O_3, our aim was to significantly enhance the nanosheets photocatalytic efficiency. Our main focus was to improve the degradation efficiency for methylene blue under visible light, which served as a representative example of a dye wastewater contaminant for our exploration. Through the successful synthesis and comprehensive characterization of 2D $Bi_2O_3/Cs_3Bi_2Br_9$, we reveal the crucial role played by the 2D structure in enhancing both the stability and photocatalytic performance of $Bi_2O_3/Cs_3Bi_2Br_9$. Finally, we investigated enhancing the S-scheme charge carrier *via* metal co-sharing.

2. Experimental section

2.1. Chemicals

Bismuth nitrate [$Bi(NO_3)_3 \cdot 5H_2O$], bismuth bromide $BiBr_3$ (97%), cesium bromide (CsBr, 99.999%, trace metals basis), isopropanol, and dimethyl sulfoxide (DMSO) were purchased from Sigma-Aldrich. Oxalic acid was purchased from Alfa Aesar. No further purification was done for any of the chemicals.

2.2. Synthesis of $Cs_3Bi_2Br_9$

The synthesis of pure $Cs_3Bi_2Br_9$ was carried out using the typical anti-solvent method. Here, in order to form a uniform $Cs_3Bi_2Br_9$ precursor solution, 192 mg of CsBr and 269.0 mg of $BiBr_3$ (molar ratio = 3 : 2)[50] were dissolved in 20 mL of DMSO. Then, 250 mL of isopropanol was quickly injected into the as-prepared precursor solution under vigorous stirring. One minute later, the obtained mixture was centrifuged at 3000 rpm for 3 min to precipitate the large particles, while the small particles were thrown out along with the solution. Then, isopropanol was added to the precipitated large particles, and the solution was centrifuged at 10 000 rpm for another 5 min. Then, the resultant sample was dried in a hot air oven at 60 °C. Finally, the pure yellow perovskite $Cs_3Bi_2Br_9$ was obtained, and was labeled as CBB.

2.3. Synthesis of Bi_2O_3

Bi_2O_3 was synthesized following the conventional hydrothermal method. Here, 20 mL of 0.1 M $Bi(NO_3)_3 \cdot 5H_2O$ and 10 mL of 1.2 M oxalic acid were slowly stirred at room temperature for 1 h. The resultant solution was sonicated for 30 min, and a white precipitate of bismuth oxalate was formed.[51] Subsequently, the precipitate was transferred into a 100 mL Teflon-lined autoclave filled with water up to 60% of its total volume. Afterwards, the autoclave was put in an oven at 150 °C for 24 h. Then, it was naturally cooled to room temperature. The obtained product was collected and washed with deionized water (DIW) and pure ethanol, and it was dried in a hot air oven at 60 °C for 2 h. Next, it was calcinated at 400 °C for 10 h to obtain the Bi_2O_3 powder, labeled as (BO).

2.4. Synthesis of $Bi_2O_3/Cs_3Bi_2Br_9$

$Bi_2O_3/Cs_3Bi_2Br_9$ was synthesized *via* the anti-solvent method. First, CsBr and $BiBr_3$ (molar ratio = 3 : 2) as well as the previously prepared pure Bi_2O_3 were dissolved in 20 mL DMSO. Several ratios of these components were used to obtain different samples. The samples comprised CsBr and $BiBr_3$, constituting 1%, 7%, 14%, 28%, and 56% of the respective composite samples, while the other part (99%, 93%, 86%, 72%, and 44%) was Bi_2O_3, respectively. Each of the resultant precursors was then sonicated for 10 min. After that, 250 mL of isopropanol was quickly injected into the as-prepared precursor solutions under vigorous stirring. The obtained samples were then centrifuged at 3000 rpm for 3 min to precipitate the large particles and then centrifuged for another 5 min at 10 000 rpm. Afterwards, the samples were dried in a hot air oven at 60 °C. Eventually, five yellow composite perovskites of $Bi_2O_3/Cs_3Bi_2Br_9$ were obtained, and were labeled as BO/CBB 1%, BO/CBB 7%, BO/CBB 14%, BO/CBB 28%, and BO/CBB 56%, based on the percentage of CBB in the composite samples (Scheme 1).

2.5. Characterization

A Rigaku Miniflex X-ray diffraction (XRD) system with Cu-Kα radiation and 40 kV/15 mA current was utilized for confirming the crystal structure of the pure Bi_2O_3 and $Cs_3Bi_2Br_9$ as well as the prepared $Bi_2O_3/Cs_3Bi_2Br_9$ composite samples. Fourier transform infrared (FTIR) spectroscopy (FTIR, SHIMADZU IRSPIRIT) (alpha model, laser class 1) was performed in the transmittance mode in the spectral range of 4000–400 cm^{-1} to identify the functional groups in crystals of the samples. A

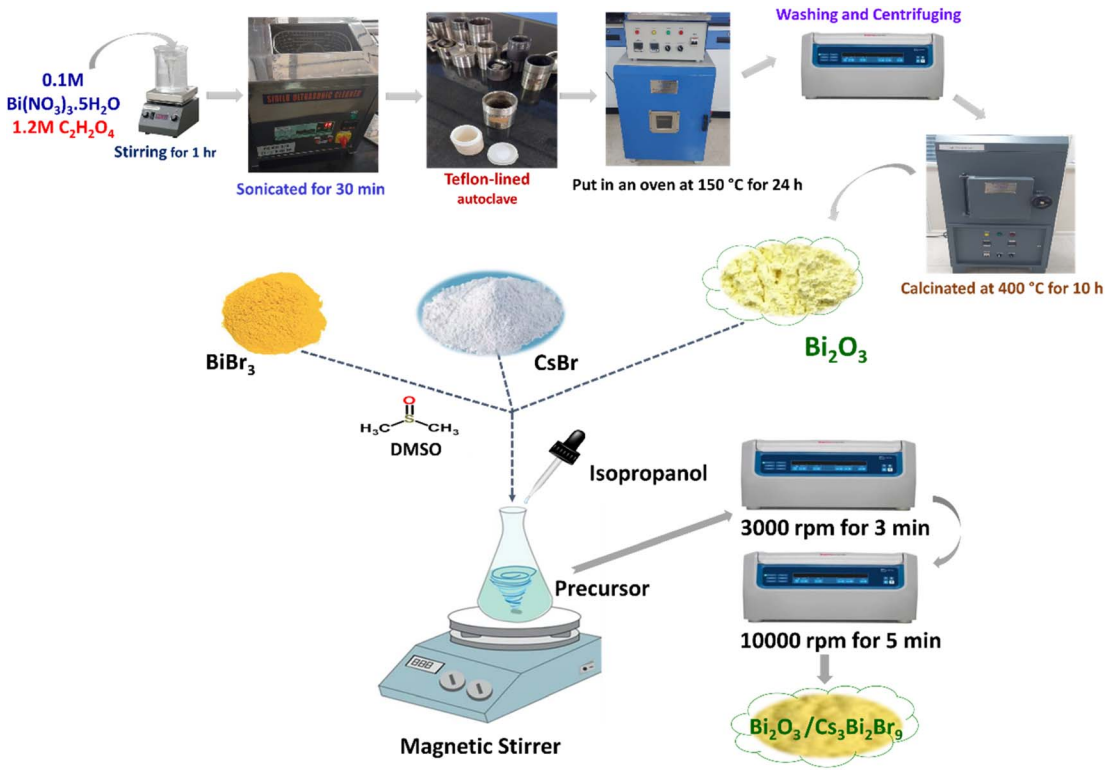

Scheme 1 Synthesis of $Bi_2O_3/Cs_3Bi_2Br_9$ nanocomposites.

Shimadzu UV-2600i instrument was employed for the UV-vis diffuse reflectance spectroscopy (DRS) measurements. Detailed information was revealed about the surface morphology of the prepared $Bi_2O_3/Cs_3Bi_2Br_9$ composite samples using scanning electron microscopy (SEM; Zeiss EVO® LS 15). Moreover, transmission electron microscopy (TEM; Talos 200 kV) was utilized to determine the size and shape of the prepared $Bi_2O_3/Cs_3Bi_2Br_9$ composite samples.

2.6. Photoreactor setup

The photocatalytic reactor used in this research work was a Heber Scientific photoreactor (Fig. S1†) from Heber Scientific (Chennai, India). This system includes a medium-pressure mercury vapour lamp (125 W, max = 365 nm) that is placed in a jacketed quartz tube. A continuous flow of cold water passes through the jacket for the purpose of dissipating the heat generated by the lamp. The dyes for testing were contained in several quartz tubes with a volume of 150 mL. These tubes have a length of 37 cm and dimensions of 2.3 cm and 2.7 cm for the inner and outer diameters, respectively. A distance of 6 cm was kept between the mercury lamp and the tubes placed around it. The catalyst particles were consistently distributed throughout the solution using an air pump.

2.7. Photocatalytic degradation of MB

A 5 ppm methylene blue (MB) solution of was individually prepared from a stock solution of MB in deionized water. The experiment was repeated three times to ensure the reliability of the results. During the experiment, the pH level of the dye solution was retained between 6.8 and 7.0 in a 100 mL volume. The dye concentration in each of the test tubes was 5 ppm. Afterwards, 10 mg of the prepared $Bi_2O_3/Cs_3Bi_2Br_9$ catalyst was added to each of the test tubes. The suspensions were stirred for 30 min in complete darkness to maintain adsorption–desorption equilibrium between the MB dye and the photocatalyst before exposing the samples to visible illumination. Subsequently, a photoreactor was utilized to irradiate the stable aqueous dye solution. A 2 mL aliquot of the photodegraded dye samples was withdrawn every 10 min, which was filtered to remove the catalysts and then centrifuged (SPINWIN, Tarsons) at 5000 rpm for 5 min. Eventually, the centrifuged suspensions were analyzed by recording the absorption band maximum of MB at 660 nm using a Shimadzu UV-2600i spectrophotometer. Eqn (1) was used to calculate the degradation efficiency.

$$\%\ \text{Degradation} = \frac{C_i - C_f}{C_i} \times 100 \quad (1)$$

where C_i and C_f are the absorbance at time zero and time t, respectively.

3. Results and discussion

3.1. PXRD patterns

Bi_2O_3 nanosheets were prepared *via* a hydrothermal method at 150 °C for 24 h. The powder X-ray diffraction (XRD) patterns are shown in Fig. 1(a and b), and reveal the good crystallinity of the structure of pristine Bi_2O_3 in a single monoclinic phase. Moreover, the observed distinct diffraction peaks of the as-prepared Bi_2O_3 could be indexed to the (002), (120), (200), (−212), (112), (−222), (041), (−321), and (−241) planes located at 2θ = 26.30°, 27.22°, 32.85°, 34.85°, 37.20°, 39.93°, 45.91°,

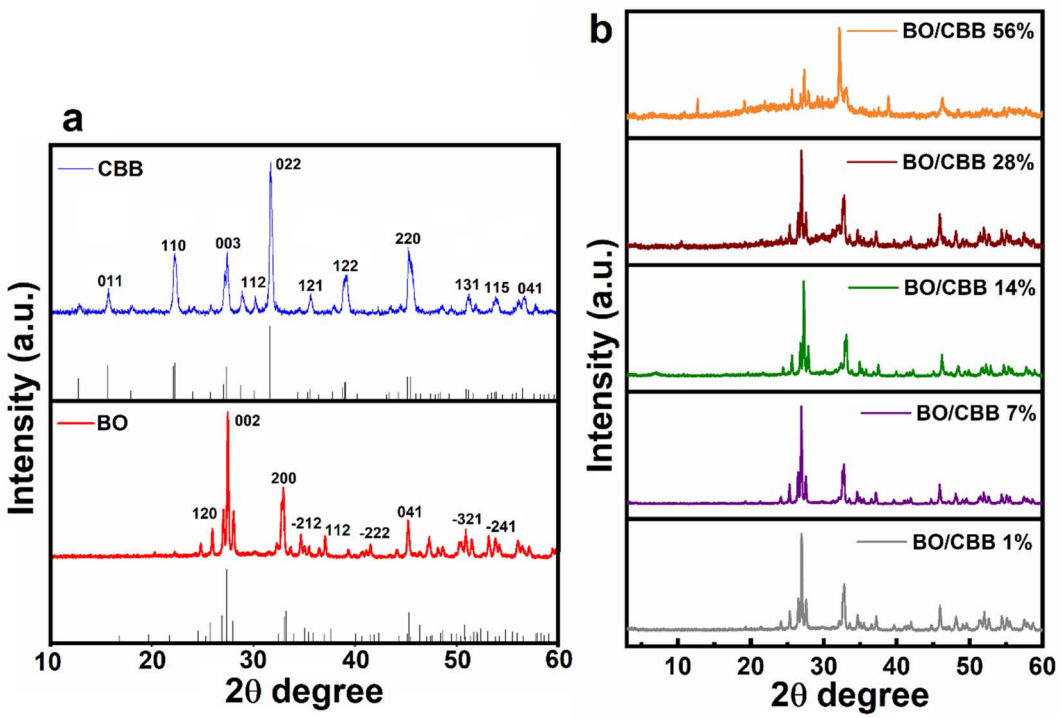

Fig. 1 XRD patterns of (a) pure BO, CBB and (b) BO/CBB 1%, BO/CBB 7%, BO/CBB 14%, BO/CBB 28%, and BO/CBB 56%.

51.89°, and 54.88°, which was in accordance with JCPDS card no. (PDF # 41-1449). The pristine $Cs_3Bi_2Br_9$ nanosheets synthesized by the anti-solvent method displayed several diffraction peaks that could be indexed to the (011), (110), (003), (112), (022), (121), (122), (220), (131), (115), and (041) planes located at 2θ = 15.60°, 22.13°, 27.22°, 28.86°, 31.76°, 35.76°, 38.83°, 45.19°, 51.01°, 53.73°, and 56.55°. The characteristics of the resultant patterns corresponded to the hexagonal phase of $Cs_3Bi_2Br_9$ and well matched the standard JCPDS card no. (PDF # 01-70-0493) with lattice parameters of $a = 7.97200$ Å, $c = 9.86700$ Å, and space group $P\bar{3}m1$.[52] $Bi_2O_3/Cs_3Bi_2Br_9$ nanosheets were fabricated following the anti-solvent method, whereby 2D $Cs_3Bi_2Br_9$ nanosheets were grown on Bi_2O_3 nanosheets based on the electrostatic interaction between Bi_2O_3 and $Cs_3Bi_2Br_9$. Evidently, the XRD patterns of the $Bi_2O_3/Cs_3Bi_2Br_9$ composites clearly displayed combination peaks for the pure Bi_2O_3 and $Cs_3Bi_2Br_9$, confirming the formation of a van der Waals heterojunction between the $Bi_2O_3/Cs_3Bi_2Br_9$ composites. The peak intensity of $Cs_3Bi_2Br_9$ increased with the increase in $Cs_3Bi_2Br_9$ content.

3.2. Fourier transform infrared spectroscopy (FTIR)

FTIR was performed to aid identifying the chemical bonds of the prepared samples (Fig. 2). For pure CBB, two peaks were observed: one at a wavenumber of around 1650 cm^{-1} corresponding to O–H (bending), and a second peak at around 3350 cm^{-1} corresponding to O–H (stretching) vibrations of residual H_2O molecules absorbed from the moisture in the environment. These matched well with the results of previous studies.[53–55] Moreover, the synthesis of BO was confirmed by the appearance of sharp bands in the range of 450–550 cm^{-1}, which were attributed to the characteristic bands for Bi–O stretching.[56] Besides, two peaks were observed centred at around 1400 and 3450 cm^{-1} related to bending and stretching of the O–H group resulting from moisture.[51] Regarding the BO/CBB composites, the peaks observed were almost in the same regions as for the pristine individual materials. It was also noticed that as the percentage of CBB increased in the composite samples, the peaks were shift towards those of pristine CBB. In general, all the characteristic peaks evidenced the formation of CBB and BO.

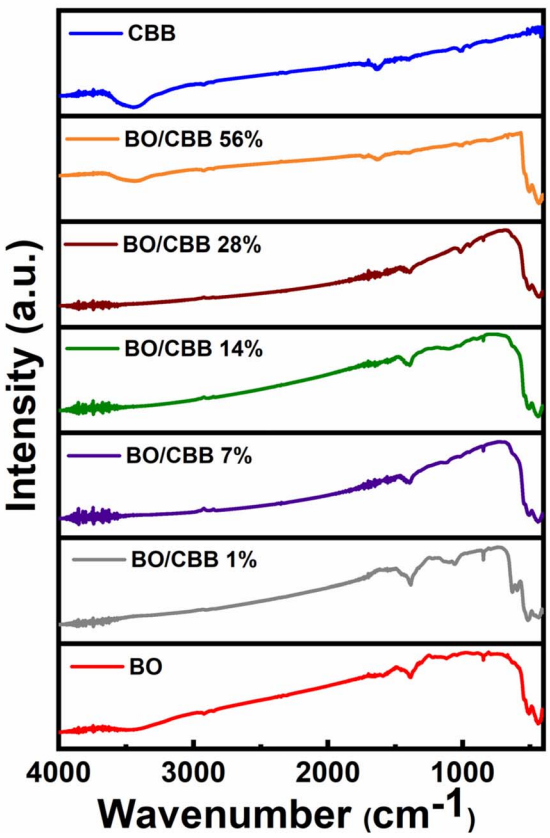

Fig. 2 FTIR spectra of BO, BO/CBB 1%, BO/CBB 7%, BO/CBB 14%, BO/CBB 28%, BO/CBB 56%, and CBB.

3.3. Field emission scanning electron microscopy (FE-SEM)

The morphology of the prepared samples was obtained in detail using FE-SEM. Large 2D nanosheet layers with smooth surfaces were clearly observed in pure CBB (Fig. 3(a)). As shown in Fig. 3(b), for the morphology of pristine BO, a grouping or stacking of 2D nanosheets with shorter dimensions than pure CBB could be observed. Regarding the composite sample BO/CBB 1%, it could be seen that the 2D nanosheets of CBB slightly interacted with BO (Fig. 3(c)). Moreover, as the ratio of CBB increased, the interaction with BO increased, until there was a complete interplay between them for BO/CBB 56% (Fig. 3(d–g)). This increase in the interaction and Bi co-sharing promoted the generation of more active sites, thus boosting the stability of the composite and enhancing the photocatalytic efficiency.[36,37,57] Additionally, it was found that the agglomeration of the five composite samples was reinforced with the increase in the interaction and Bi co-sharing between BO and CBB.

3.4. Energy-dispersive X-ray (EDX) spectroscopy

EDX is an analytical technique that is utilized for determining the elemental analysis and chemical characterization of samples using an electron microscope. Fig. 4 shows the EDX spectrum of the composite sample BO/CBB 28%, which confirmed the presence of Cs, Bi, Br, and O elements.

3.5. Transmission electron microscopy (TEM) and selected area electron diffraction (SAED)

The morphology of the BO/CBB 28% composite was investigated by TEM, with the TEM image displaying the formation of 2D nanosheets with slight agglomeration, high crystallinity, and in close contact with each other, as shown in Fig. 5(a). Moreover, the images obtained from high-resolution TEM (HRTEM) revealed stacked nanosheets that had lattice fringes with *d*-spacings of 0.26 and 0.32 nm, corresponding to the (022) crystal plane belonging to CBB and (120) plane belonging to BO, respectively (Fig. 5(b–d)). Strong interaction resulting from Bi co-sharing was thus observed between the individual components of the composite. Furthermore, the SAED pattern indicated the existence of bright spots, with the lattice fringes

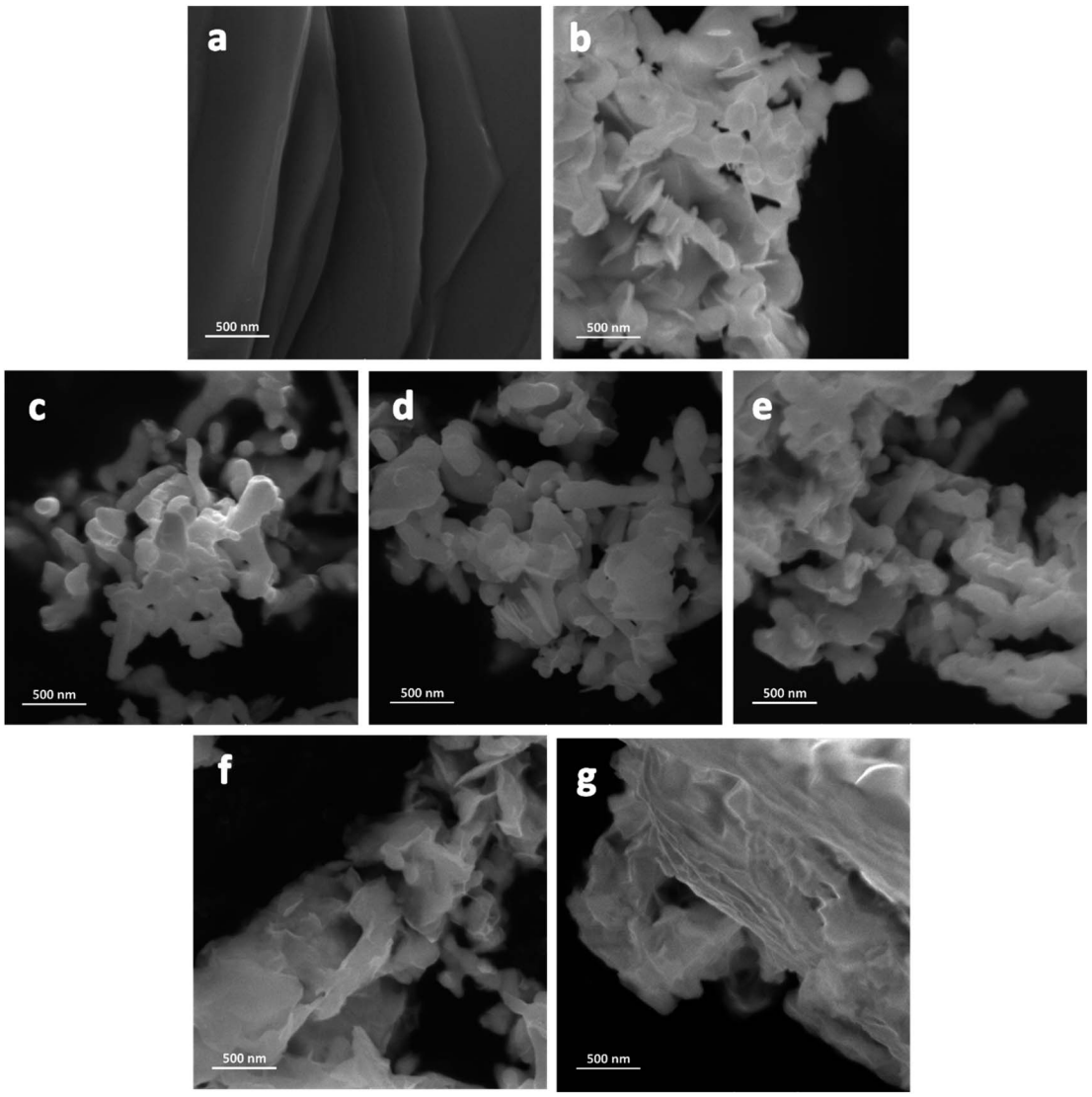

Fig. 3 SEM images of (a) CBB, (b) BO, (c) BO/CBB 1%, (d) BO/CBB 7%, (e) BO/CBB 14%, (f) BO/CBB 28%, and (g) BO/CBB 56%.

spacings corresponding to the (110) and (022) crystal planes of CBB and (120) plane of BO (Fig. 5(e)). Some defects in the lines of the lattice fringes could also be noticed (Fig. 5(c and d)), indicating the presence of oxygen vacancies (OVs).[58] These results were in excellent agreement with the planes found in the PXRD pattern. The STEM-EDS elemental mapping images exhibited a homogeneous elemental distribution of Cs, Bi, Br, and O, as displayed in Fig. 6.

3.6. Surface elemental analysis

The surface chemical composition, as well as the electronic states of the two pure synthesized samples (BO and CBB) and the optimal composite (BO/CBB 28%), were investigated by XPS to understand the possible charge migration pathways in the heterostructure (Fig. 7). The shift of the peak position was calibrated according to the binding energy of C 1s at 284.6 eV.[59] The survey spectra of BO, CBB, and BO/CBB 28% were compared, as shown in Fig. S2.† Moreover, high-resolution XPS (HR-XPS) was performed on Cs, Br, Bi, and O to obtain more detailed information about the chemical state of the resultant heterostructure. In Fig. 7(c), two peaks could be observed at 724.0 and 738.0 eV (Cs 3d) related to Cs $3d_{5/2}$ and Cs $3d_{3/2}$ in CBB, and two peaks at 724.2 and 738.2 eV (Cs 3d) related to Cs $3d_{5/2}$ and Cs $3d_{3/2}$ in the BO/CBB 28% composite, indicating a slight positive shift compared with the pure CBB. Similarly, for Br 3d, Fig. 7(b) shows a peak at 68.5 eV for CBB, and at 68.7 eV for the BO/CBB 28% composite, demonstrating a positive shift compared with the pure CBB. These slight positive shifts in the Cs 3d and Br 3d peaks of the BO/CBB 28% composite indicate the migration of electrons from CBB and the generation of an internal electric field at the interface, which resulted in an upward bending of its potential energy level, thereby facilitating the formation of an S-scheme junction.[60,61] Fig. 7(a) shows the binding energies in the spectrum of the Bi 4f core level; for the BO/CBB 28% composite, two peaks were observed located at 159.6 and 164.6 eV, ascribed respectively to Bi $4f_{7/2}$ and Bi $4f_{5/2}$

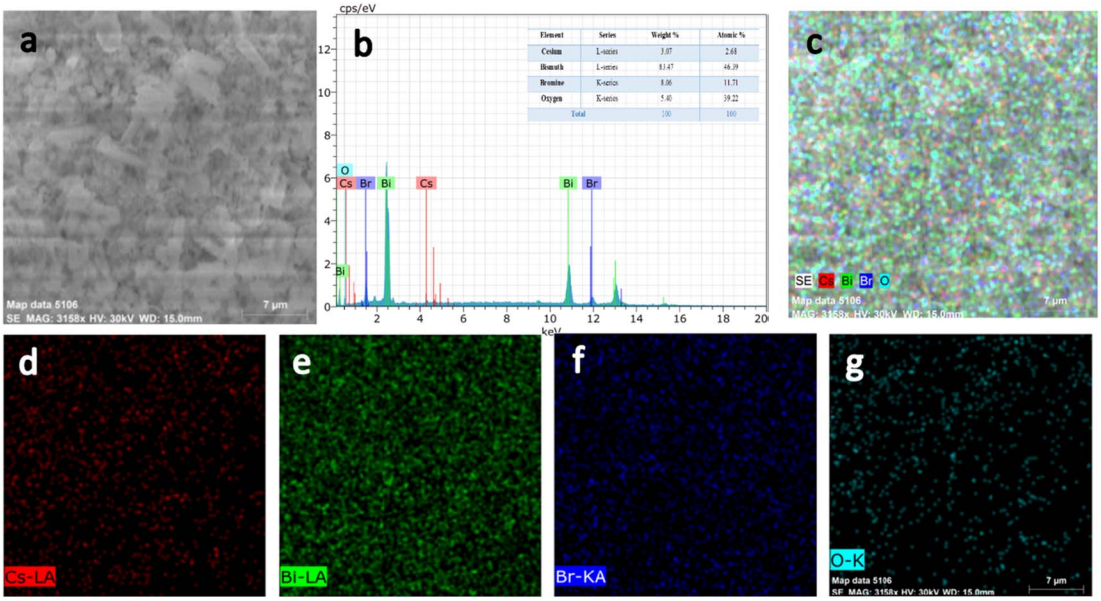

Fig. 4 BO/CBB 28% (a) SEM image, (b) EDX analysis, and (c–g) elemental mapping analysis.

Bi^{3+} oxidization states.[62] Similarly, Bi $4f_{7/2}$ and Bi $4f_{5/2}$ displayed peaks at 159.3 and 164.9 eV for CBB and at 159.9 and 165.1 eV for BO (Fig. 7(a)). The Bi 4f binding energies of CBB and BO showed a remarkable negative and positive shift, respectively, compared with the BO/CBB 28% composite. These positive and negative shifts in the Bi 4f of CBB and BO indicate the transfer of electrons from CBB to BO during their junction formation and the upward and downward bending of their energy potentials, respectively. Moreover, these remarkable shifts in the Bi 4f core level confirmed the strong interaction between CBB and BO in the heterojunction, indicating there was Bi interfacial co-sharing between BO and CBB due to the equilibrium of their Fermi levels. The formation of such a Bi interfacial co-sharing metal bond between CBB and BO would enhance the heterojunction stability and the charge transformations. These observations were also observed in the O 1s spectrum of the pure BO in comparison to BO/CBB 28% (Fig. 7(d)). It was also observed the intensity of the O 1s spectrum in the pure BO was higher than in BO/CBB 28%, indicating the lower content number of O atoms in the BO/CBB 28% composite and metal surface exposure between the CBB and BO components. The O 1s spectrum for pure BO showed two prominent peaks at 529.6 and 531.3 eV related to the Bi–O bond and oxygen vacancies (OVs).[58,63] These OVs in BO would facilitate the formation of Bi–Bi bonds between CBB and BO during the formation of the BO/CBB 28% composite. From the O 1s core level of the BO/CBB 28% composite, it could be observed the ratio of OVs and Bi–O was remarkably reduced, which indicated the filling of these vacancies by the Bi atom and the replacement of the Bi–O bond by a Bi–Bi bond. However, the additional peak located at 531.5 eV in the O 1s spectrum of BO/CBB 28% was ascribed to the hydroxyl (OH) group on the surface due to the humidity sensitivity of CBB. Moreover, it could be observed that the peak for Bi–O in BO/CBB 28% showed a negative shift compared to in BO, which further verified the Bi replacement and acquisition of a negative charge on the BO surface at the interface with CBB in the heterojunction. Ultimately, these shifts facilitated the formation an S-scheme junction, whereby interfacial Bi atom co-sharing between CBB and BO greatly boosted the S-scheme charge transfer, maintaining a high charge separation and efficient photocatalytic degradation.[61,64]

As can be seen from Fig. 7(d), there were two prominent peaks at 529.6 and 531.3 eV in the O 1s spectrum of BO, which were related to Bi–O bonds and OVs, while three peaks could be observed at 528.4, 529.9, and 531.5 eV in the O 1s spectrum of the BO/CBB 28% composite, which were related to Bi–O, OVs, and hydroxyl group bonds, indicating a positive shift compared with the pure BO. Moreover, the intensity of the O 1s spectrum was noticeably higher in the pure BO than in BO/CBB 28%. This decrease in the O 1s spectrum intensity of the composite was due to the replacement of O 1s by bismuth, where Bi-sharing was formed instead of Bi–O. Additionally, there were more OVs in the composite. A shift was thus noticed, referring to the replacement of O 1s by Bi. Based on the above analyses, it could be concluded that Bi had replaced O 1s in BO/CBB 28% with atomic-level contact enabled by Bi atom co-sharing.[64] These resulting positive and negative shifts of the binding energy signified the electronic density degree.[59] As such, an internal electric field was generated at the interface of BO/CBB 28%, which facilitated the smooth migration of electrons from the CBB phase across the interface to the BO phase. Hence, this interfacial Bi atom co-sharing between CBB and BO greatly boosted the S-scheme charge transfer due to their effective spatial charge separation, maintaining a high-efficiency photocatalytic degradation.[64]

3.7. UV-vis-diffuse reflectance spectroscopy

The photophysical properties of the prepared pure and composite samples were studied by UV-vis-DRS, as shown in Fig. 8(a). The BO, BO/CBB 1%, BO/CBB 7%, BO/CBB 14%, BO/

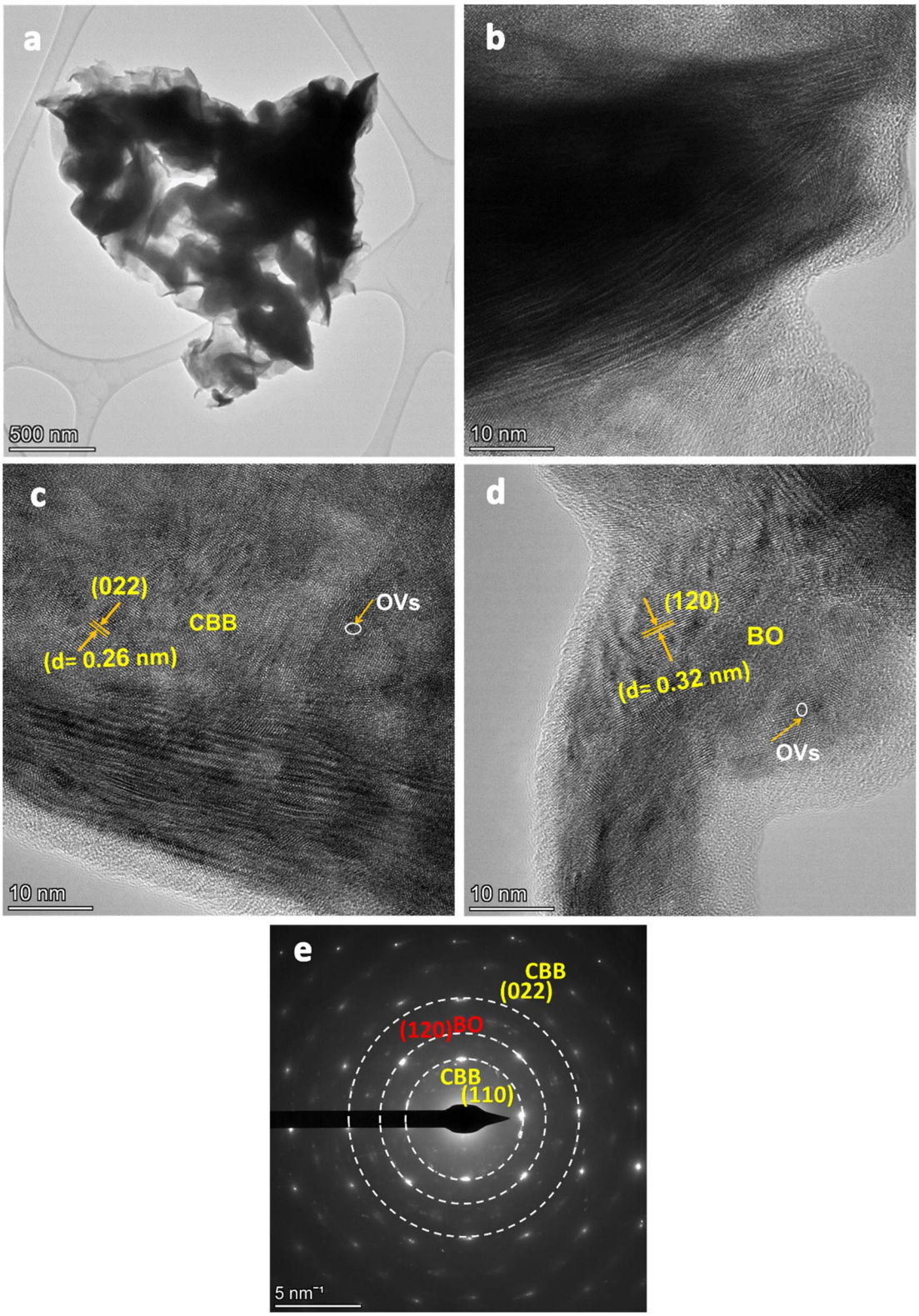

Fig. 5 TEM images (a and b), high-resolution (HR)-TEM images (c and d), and SAED pattern (e) of the BO/CBB 28% composite.

CBB 28%, BO/CBB56%, and CBB samples absorbed visible light at around 461, 459, 453, 456, 456, 449, and 442 nm, respectively. The following equation was used to calculate the band gap energy.[65]

$$(\alpha h\nu)^{\gamma} = K(h\nu - E_g) \quad (2)$$

where K is a constant called the band tailing parameter, and E_g is the energy of the optical band gap. Fig. 8(b) shows the Tauc

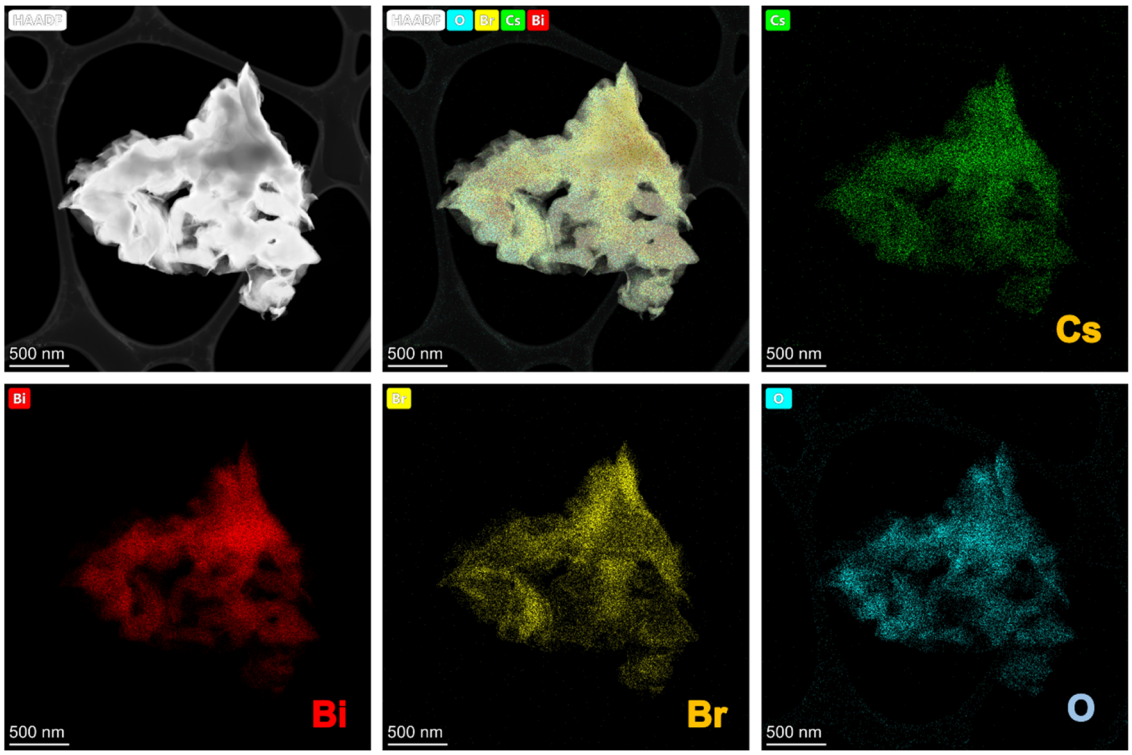

Fig. 6 STEM-EDS mapping of Cs, Bi, Br, and O in the BO/CBB 28% composite.

plots for the band energy. The band gap energies of the synthesized BO, BO/CBB 1%, BO/CBB 7%, BO/CBB 14%, BO/CBB 28%, BO/CBB 56%, and CBB were 2.45, 2.44, 2.47, 2.46, 2.46, 2.49, and 2.54 eV, respectively. BO and BO/CBB 1% showed the lowest band gaps among the seven samples. Fig. 8(a) reveals that BO/CBB 28% and BO/CBB 56% had higher absorption rates, owing to the increase in the active sites generated by the strong interaction between CBB and BO, hence increasing the photocatalytic activity.

3.8. Evaluation of the photocatalytic activity of MB

The photocatalytic efficiency of BO, BO/CBB 1%, BO/CBB 7%, BO/CBB 14%, BO/CBB 28%, BO/CBB56%, and CBB was assessed *via* observing their ability to degrade MB in the dark and under visible light, and the obtained results are displayed in Fig. 8. The experiments were conducted by dissolving 10 mg of each of the prepared photocatalyst samples in a 100 mL solution containing the MB dye concentration of 5 ppm. The total time for the degradation was 90 min (30 min in the dark and 60 min under visible light). Initially, the experiments were carried out in the dark. It was found that the dye did not undergo any significant degradation in any of the samples, which well matched with the results of previous studies.[66,67] Still, a very slight degradation of the dye was noticed in the first 30 min, which could be attributed to the adsorption of MB on the photocatalyst surface. Subsequently, the dye concentration remained unchanged. Under visible illumination, the degradation rate was reported at definite time intervals (10 min) for each of BO, BO/CBB 1%, BO/CBB 7%, BO/CBB 14%, BO/CBB 28%, BO/CBB56%, and CBB. Regarding the pure catalysts BO and CBB, there was no significant change in the MB concentration (~40% and ~35%, respectively) during the time of the experiment.

With respect to the composite samples, the degradation rate increased with the increase in the CBB content, until reaching BO/CBB 28%. Beyond this, the degradation rate started decreasing. BO/CBB 28% achieved the highest percentage of MB removal among all the synthesized samples, reaching ~92%. This could be attributed to the optimal mixing percentage between the 2D nanosheets of both BO and CBB, whereupon there was a great interaction between the two components. This interaction allowed for a greater stability of the photocatalyst as well as providing an appropriate surface area, which contributed to enhancing the photocatalytic activity. Further, the increase in the percentage of 2D nanosheets of CBB (BO/CBB 56%) led to a greater interaction with BO, resulting in Bi co-sharing and leading to a reduction in the effects from the optical properties of BO. Moreover, more agglomeration was observed (as can be seen in the SEM images in Fig. 3(g)), leading to the reduction of the surface area for contact between the catalyst and the dye molecules. Hence, the photocatalytic degradation ratio started to decrease. This was consistent with the characterization results.

Typically, the degradation kinetics can be studied using two equations, namely pseudo-first-order and second-order kinetics equations, as shown below.[68]

$$-\ln(C_i/C_0) = k_1 t \quad (3)$$

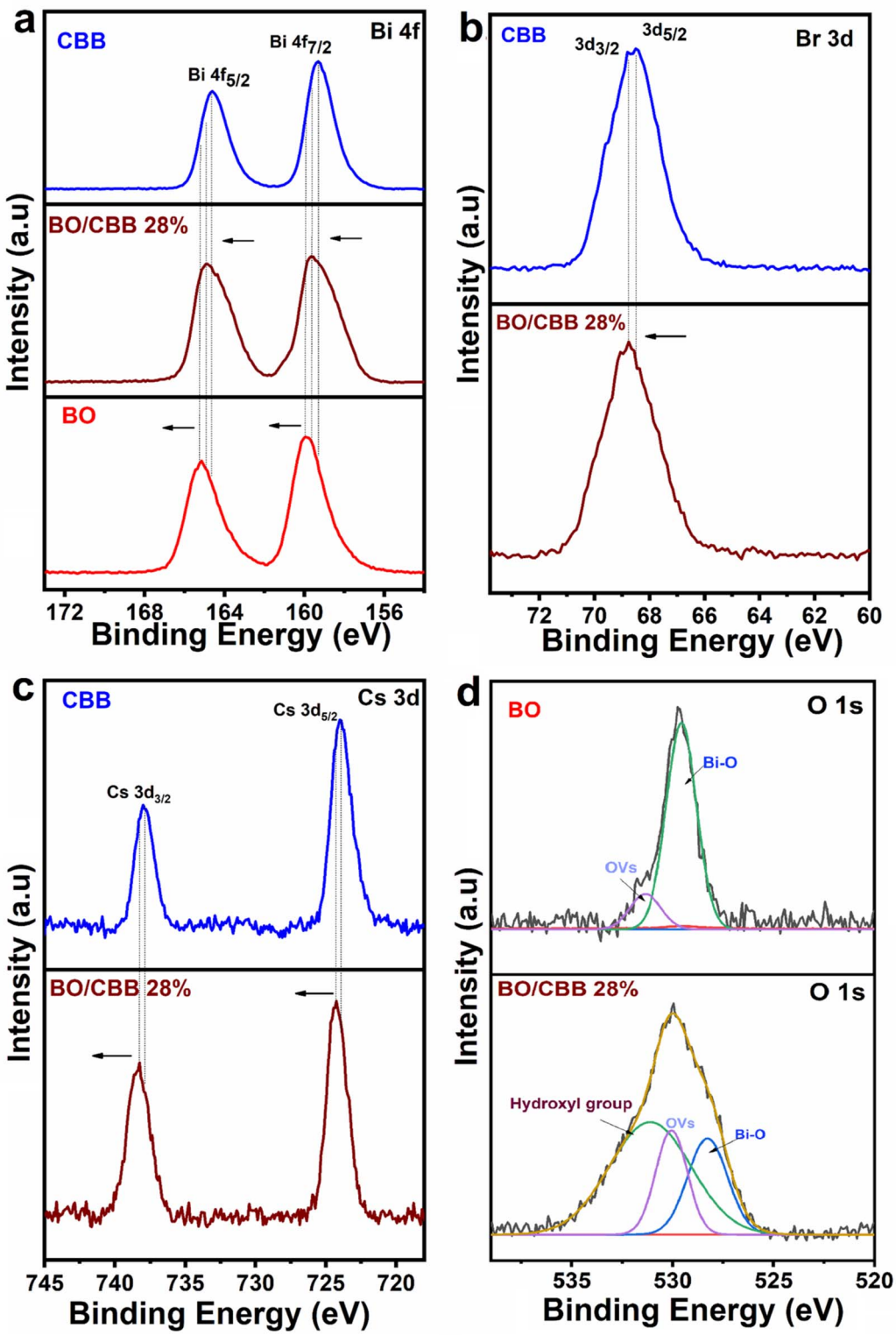

Fig. 7 High-resolution (a) Bi 4f, (b) Br 3d, (c) Cs 3d, and (d) O 1s XPS spectra of BO, BO/CBB 28%, and CBB.

$$1/(C_i - C_f) = 1/(C_0 - C_f) + k_2 t \quad (4)$$

where C_f is the MB equilibrium concentration at time t, C_0 and C_i are the MB concentration at time $t = 0$, and k_1 and k_2 are the first-order and second-order kinetic rate constants, respectively.

Both Fig. 9(b) and Table 1 display the kinetics of the BO, BO/CBB 1%, BO/CBB 7%, BO/CBB 14%, BO/CBB 28%, BO/CBB56%, and CBB photocatalysts for the degradation of MB under visible light irradiation. The reaction constant k was found to be 0.00776, 0.00813, 0.00977, 0.02378, 0.03841, 0.0294, and

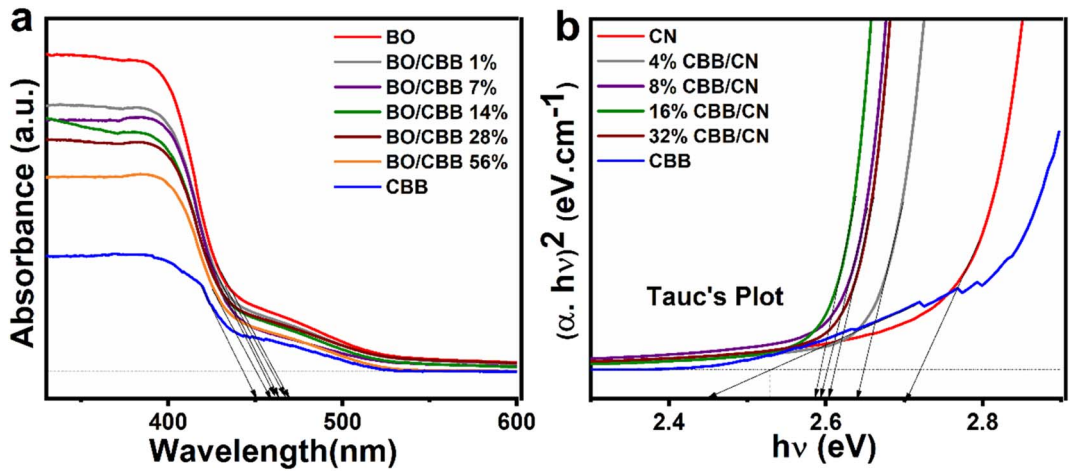

Fig. 8 (a) UV-vis-DRS plots and (b) band gap energy Tauc plots of BO, BO/CBB 1%, BO/CBB 7%, BO/CBB 14%, BO/CBB 28%, BO/CBB 56%, and CBB.

0.00671 min^{-1} for the aforementioned photocatalysts, respectively. Additionally, the process could be described by a pseudo-first-order kinetic model with R^2 values of 0.9326 for BO, 0.95227 for BO/CBB 1%, 0.9716 for BO/CBB 7%, 0.89608 for BO/CBB 14%, 0.90362 for BO/CBB 28%, 0.94644 for BO/CBB 56%, and 0.93079 for the CBB photocatalysts.

The photodegradation pathway of MB degradation with BO/CBB 28% (0.1 g L^{-1}) under visible light was investigated through mass spectroscopy (MS), and the proposed route is shown in Fig. 10. The MS spectrum of MB dye had corresponding fragments at m/z 284, 303, 201, 215, 157, and 142, which well conformed with the previous studies.[69,70] At m/z 303,

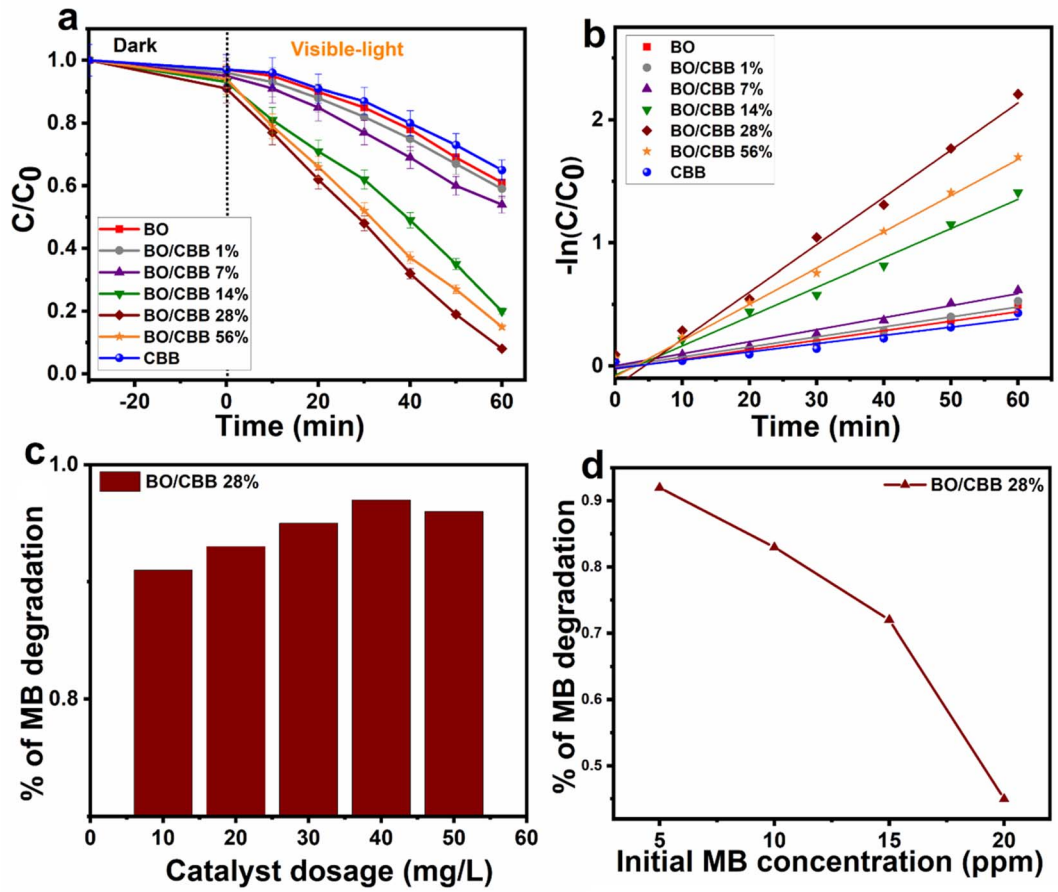

Fig. 9 (a) Degradation curves, (b) kinetics of the photodegradation, (c) catalyst dosage effect, and (d) effect of the initial MB concentration.

Table 1 Slope of $-\ln(C/C_0)$ against time for BO, BO/CBB 1%, BO/CBB 7%, BO/CBB 14%, BO/CBB 28%, BO/CBB 56%, and CBB photocatalysts in the MB degradation process

Equation	$y = a + bx$		
Sample	Intercept	Slope	Adj. *R*-square
BO	-0.02388 ± 0.03054	$0.00776 \pm 8.4711 \times 10^{-4}$	0.9326
BO/CBB 1%	-0.00737 ± 0.02668	$0.00813 \pm 7.3987 \times 10^{-4}$	0.95227
BO/CBB 7%	0.0022 ± 0.02453	$0.00977 \pm 6.80438 \times 10^{-4}$	0.9716
BO/CBB 14%	-0.07405 ± 0.11809	0.02378 ± 0.00328	0.89608
BO/CBB 28%	-0.16746 ± 0.18302	0.03841 ± 0.00508	0.90362
BO/CBB 56%	-0.08657 ± 0.10246	0.0294 ± 0.00284	0.94644
CBB	-0.01924 ± 0.02675	$0.00671 \pm 7.4189 \times 10^{-4}$	0.93079

a new peak was observed, which may indicate the cleavage/oxidation of the substituted dimethyl groups in both imines for MB.[71] Thus, CBB250 had a higher efficiency for decolorizing and degrading the entire structure of MB dye under visible light.

3.8.1. Catalyst dosage. The catalyst dosage is an influential parameter that has a significant impact on the mechanism of pollutant degradation.[20,72–74] In the current study, the optimal obtained sample (BO/CBB 28%) was further studied with respect to catalyst loading, whereby different BO/CBB 28% concentrations ranging from 10 to 50 mg L^{-1} were tested. Based on the experiments conducted in the current study, the results demonstrated that the photocatalytic efficiency increased as the concentration of the catalyst increased from 10 to 40 mg L^{-1}. However, a decline in MB degradation was noticed beyond this concentration rate. Evidently, the enhanced photocatalytic activity was largely influenced by both charge separation and light absorption. The increase in the photocatalytic degradation was attributed to an increase in the active sites on the photocatalyst surface. The optimal degradation rate occurred as the concentration of BO/CBB 28% reached a 40 mg L^{-1} catalyst concentration dosage, whereby the removal of MB was almost 96% within 60 min. However, as the catalyst loading was further increased, the ratio of light penetration was impaired (Fig. 9(c)). As such, the number of generated active sites on the catalyst surface was reduced due to light diffraction caused by the excessive catalyst loading, thus inhibiting dye degradation.[75]

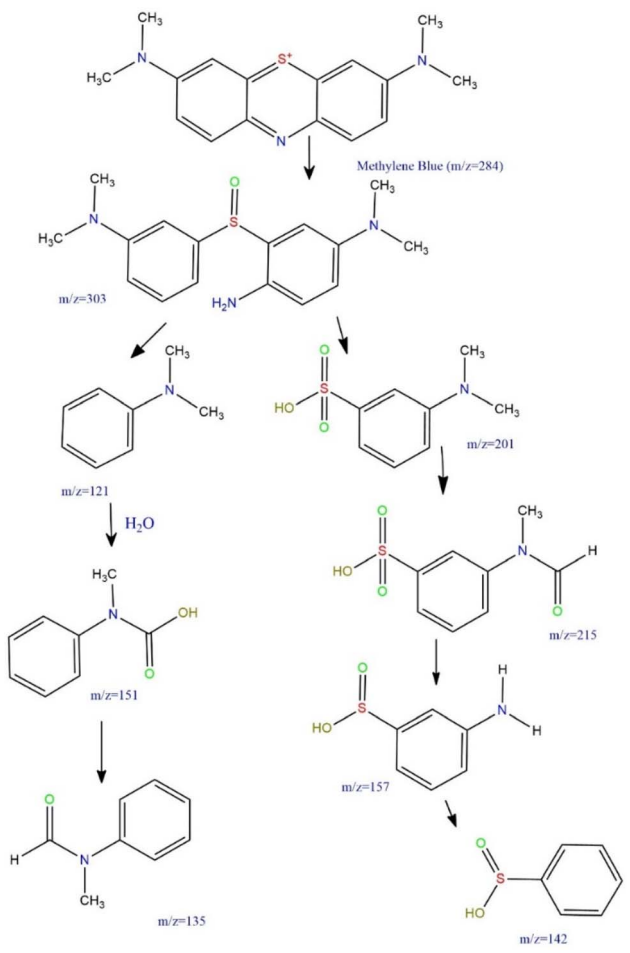

Fig. 10 MB degradation pathway during photocatalysis.

3.8.2. Initial MB concentration. The photodegradation efficiency of BO/CBB 28% nanosheets was studied with reference to the initial MB concentration. Several initial concentration rates of MB were tested ranging from 5 to 20 ppm under 60 min visible light irradiation. The results indicated that increasing the initial MB concentration caused a decline in the photocatalytic degradation efficiency (Fig. 9(d)). This was ascribed to the presence of more particles around the active sites of the photocatalyst, hence, the light was impeded from passing through the surface of the catalyst, limiting the generation of e^-/h^+ pairs. As a result, the photocatalytic degradation efficiency dropped.[76] The effect of pH on the degradation of MB by the optimal BO/CBB 28% composite was also studied, with the discussion of this and the result provided in the ESI file.†

3.8.3. Photocatalytic stability. The photostability and the reusability of the two pure prepared samples (*i.e.*, BO and CBB), and the two optimal prepared composite samples regarding dye degradation (*i.e.*, BO/CBB 28% and BO/CBB 56%) were further evaluated by filtering, collecting, rinsing, and reusing the photocatalysts for four cycling experiments, as shown in Fig. 11. Although the pure photocatalysts (BO and CBB) showed low degradation activity during the first round compared to the composite samples, they almost maintained their degradation rate during the next four cycles, without showing any remarkable decline. Interestingly, the composite photocatalysts (BO/

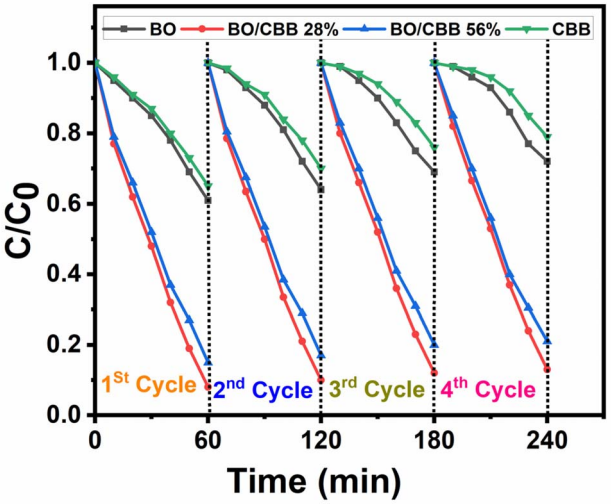

Fig. 11 Stability tests based on the photocatalytic degradation of MB in four catalytic cycles using BO, BO/CBB 28%, BO/CBB 56%, and CBB.

CBB 28% and BO/CBB 56%) exhibited no apparent loss in their photocatalytic activity after the four test cycles. The very slight decrease in their activity that was seen might be partially attributed to the loss of photocatalytic particles caused by the collection and washing during each testing cycle as well as due to photocorrosion.[77,78] Thus, it was demonstrated that the catalysts could retain their photocatalytic properties over time, and were chemically stable under these conditions. Among all of the studied photocatalysts in this research work, BO/CBB 56% presented slightly better stability compared to BO/CBB 28%; still, the latter composite showed better overall performance regarding efficient photocatalytic degradation. The stability of BO/CBB 28% was further proved by the XRD results before and after the photocatalytic recycle tests (Fig. S4†). A slight reduction in the peaks was observed after the fourth cycle though, which was ascribed to photocorrosion.[77]

3.8.4. Pollutant degradation mechanism. The band structures of CBB and BO were analysed in order to trace their photocatalytic mechanism. The work function was calculated using XPS measurements with a negative applied bias of −29.4 eV. Based on the work function, the Fermi levels of the samples were found to be situated at −3.7 eV for CBB and −5.6 eV for BO, as shown in Fig. 12(a). For the purpose of estimating the energy between the Fermi level and the valence band edge of each semiconductor, valence-band XPS measurements were calculated, as exhibited in Fig. 12(b). Hence, the construction of the energy diagrams for CBB and BO was performed based on linking the findings with the previously calculated band gaps (2.54 eV for CBB and 2.45 eV for BO), whereupon the conduction band of CBB was found to be −3.1 eV, and that of BO was found to be −4.28 eV (Fig. 12(d)). The Fermi level of CBB was higher than that of BO. As such, electrons would travel from CBB to BO, generating an internal electric field from BO to CBB.[79] A remarkable charge density barrier that would improve the charge transfer has the potential of being created due to this junction. Additionally, the different Fermi energy levels possessing thermal equilibrium led to the alignment of the valence band (VB) and conduction band (CB), resulting in an upward rise of the CBB energy bands, and a downward movement of the BO energy bands. Consequently, an S-scheme heterojunction was formed.[80,81] Positive charges accumulated in CBB, and negative ones in BO in the depletion layer.

As the catalyst sample was exposed to light, electrons travelled from the VB to the CB of both CBB and BO, leading to the generation of holes behind them. The internal electric field from BO to CBB and the band bending resulting from the Coulomb force can preserve the photogenerated electrons on the CBM of CBB, and the holes on the VBM of BO with a higher redox potential. The electrons on the CBM of BO would quickly recombine with the holes on the VBM of CBB, as these holes would be closer to the electrones on the CBM of BO than the holes present on the VBM of BO, hence leading to charge-carrier separation with maximized redox potentials (Fig. 12(f)). Hence, the establishment of the S-scheme heterojunction was ascertained.[82–84]

Furthermore, the photocatalytic mechanism was investigated to determine the main active species, whereupon radical-trapping experiments were conducted under optimal conditions *via* the utilization of several suitable scavengers for each species, namely benzoquinone (BQ), potassium dichromate ($K_2Cr_2O_7$), ethylene diamine tetra acetic acid disodium (EDTA-2Na), and methanol (MeOH) for $^{\bullet}O_2^-$, e^-, h^+, and $^{\bullet}OH^-$, respectively.[84–87] Fig. 12(c) shows that when $K_2Cr_2O_7$ and BQ were utilized as scavengers, the photodegradation of MB was significantly decreased, with BQ exhibiting a lower photodegradation rate. The use of MeOH led to an approximately 50% decrease in MB photocatalytic degradation. Eventually, the addition of EDTA-2Na resulted in a slight MB degradation decrease. These results reveal that the holes hardly affected the degradation performance of MB. Superoxide oxygen radicals and electrons played the most significant role in the degradation process of MB, while the superoxide hydroxyl radicals had a less noticeable effect on the degradation process of MB by $Bi_2O_3/Cs_3Bi_2Br_9$.

To demonstrate the formation of an S-scheme heterojunction in the BO/CBB 28% heterostructure, electron spin resonance (ESR) measurements were carried out with 5,5-dimethyl pyrroline *N*-oxide (DMPO) as a spin-trapping agent to identify the generation of $^{\bullet}OH$ and $^{\bullet}O_2^-$ radicals in water and alcohol solutions, respectively.[88] BO/CBB 28% exhibited robust ESR signals for both radicals in both media, while BO produced only $^{\bullet}OH$ in water and CBB produced only $^{\bullet}O_2^-$ in alcohol solution (Fig. 12(d and e)). These results indicate that the generated electrons in the BO/CBB 28% gathered in the CB of CBB for efficient $^{\bullet}O_2$ generation, while the holes accumulated on the VB of BO for $^{\bullet}OH$ production. This charge separation differs from that observed in traditional type-II junctions, further evidencing the formation an S-scheme heterojunction. This unique charge migration pathway underpins the enhanced photocatalytic performance of the BO/CBB 28% heterostructure in degrading MB. The ESR results were consistent with the XPS

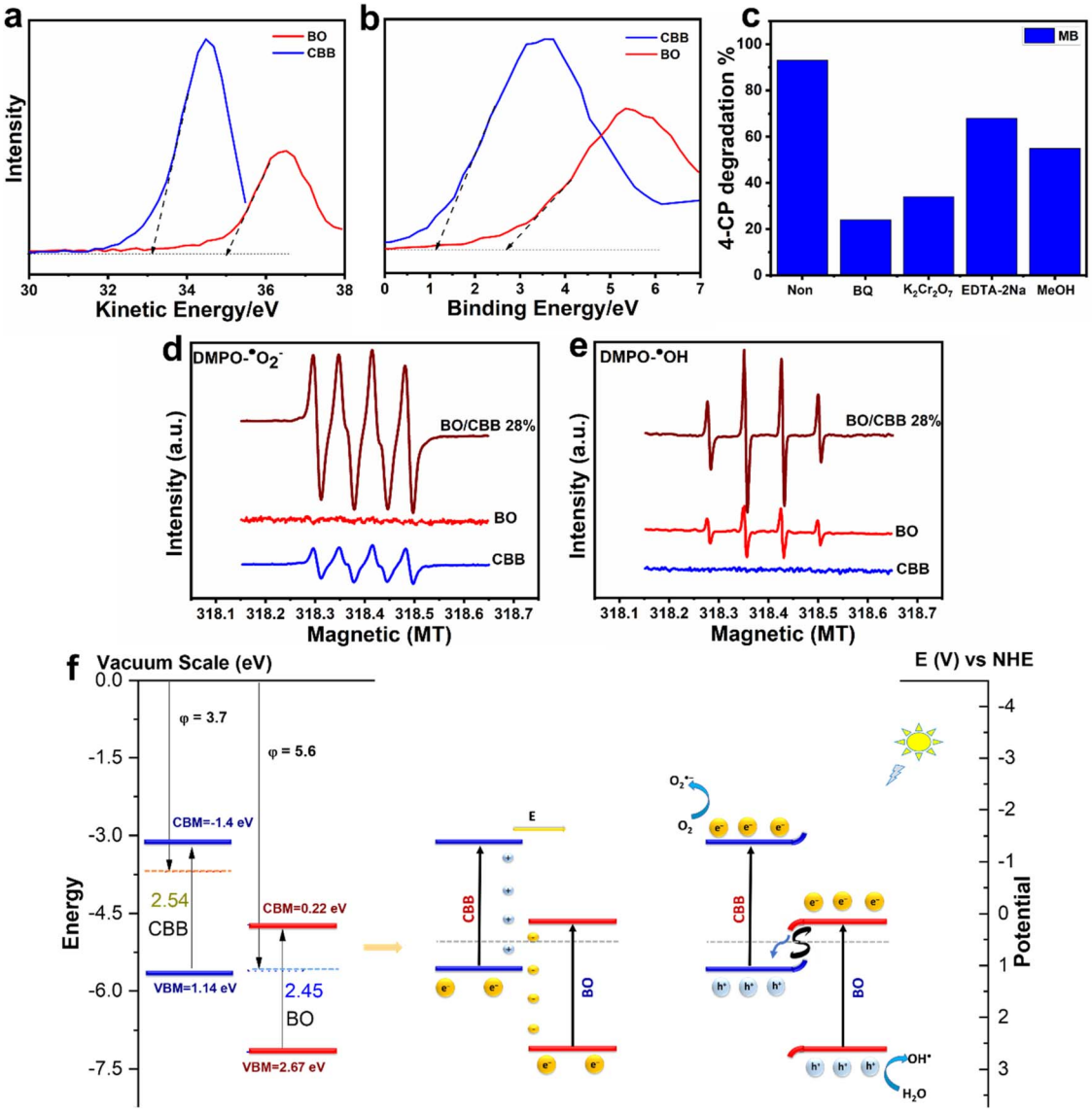

Fig. 12 (a) Work function. (b) Valence-band edge measurements using valence-band XPS for CBB and BO. (c) Scavenger experiments with various scavengers (for MB degradation over BO/CBB 28%). (d) 5,5-Dimethyl-1-pyrroline *N*-oxide (DMPO) spin-trapping electron paramagnetic resonance (EPR) spectra of $^{\bullet}OH$, and (e) DMPO–$^{\bullet}O_2^-$, (f) conduction and valence-band edge positions and Fermi levels of the two pure semiconductors, and schematic of the reaction mechanism.

and scavenger test results, supporting the suggested charge-transfer mechanism.

4. Conclusion

The current study successfully delved into the fabrication and characterization of a novel bismuth-halide-perovskite-based nanocomposite photocatalyst with different ratios of Bi_2O_3/$Cs_3Bi_2Br_9$ prepared *via* the anti-solvent method. The $Cs_3Bi_2Br_9$ percentages in the composites were 1%, 7%, 14%, 28%, and 56% to obtain BO/CBB 1%, BO/CBB 7%, BO/CBB 14%, BO/CBB 28%, and BO/CBB56%, respectively. The resultant samples were compared with each other with respect to their optical properties, morphology, stability, and photocatalytic degradation performance. Moreover, they were also compared with pristine 2D Bi_2O_3 and 2D $Cs_3Bi_2Br_9$ nanosheets. The SEM images confirmed the formation of 2D nanosheets of the two pure samples. Further, the results affirmed that increasing the ratio of $Cs_3Bi_2Br_9$ in the composites led to an increase in the interaction with Bi_2O_3 owing to Bi co-sharing, thus boosting the stability of the synthesized composites in aqueous medium. However, the further increase in the percentage of $Cs_3Bi_2Br_9$ hindered benefiting from the optical properties of Bi_2O_3 as there was greater agglomeration, thus leading to a smaller surface area and resulting in a decrease in the photocatalytic degradation. BO/CBB 28%, which had a band gap of 2.46 eV, exhibited the optimal degradation rate for MB, reaching ~92% within 60 min. This mixing ratio between Bi_2O_3 and $Cs_3Bi_2Br_9$ allowed for taking advantage of the beneficial properties of both

2D Bi_2O_3 and 2D $Cs_3Bi_2Br_9$. Besides, appropriate stability was achieved along with a large surface area-to-volume ratio, providing ample active sites that are essential for irradiation absorption. Also, the contact between the catalyst and the target pollutant molecules was intensified because of the interfacial co-sharing of Bi atoms, while the internal electric field facilitated the development of an improved S-scheme heterostructure. As such, the catalytic degradation efficiency was enhanced. In addition, the photocatalytic dosage of 40 mg L^{-1} was proven to be the optimal dosage in terms of the efficiency of pollutant degradation. The initial dye concentration also affected the degradation efficiency, whereby raising the initial concentration of the dye led to a decrease in degradation efficiency. Furthermore, scavenger experiments indicated that both $^{\bullet}O_2^-$ and e^- played the most important role in the removal of MB. The current study proposes a novel composite of a metal halide perovskite coupled with bismuth oxide for the purpose that can improve the catalyst stability and enhance the photocatalytic degradation efficiency in aqueous medium. Future research work may further study Bi co-sharing as well as coupling metal halide perovskites with other metal oxides for the purpose of ascertaining the optimal composites for photocatalytic degradation.

Data availability

The data utilized in this study will be made available upon request.

Author contributions

Mohamed Masri: conceptualization, data curation, methodology, writing – original draft, discussion, investigation, proofreading, writing – reviewing, editing, and formal analysis. Girisha K. B.: supervision, investigation, and discussion. Abdo Hezam: conceptualization, writing-reviewing, discussion, and editing. Talal F. Qahtan: discussion and editing. Khaled Alkanad: discussion, formal analysis, and proofreading. Qasem A. Drmosh: discussion and funding. Faten Masri: discussion, and editing. Kalappa Prashantha: discussion. Manjunath S. H.: discussion. Sanaa Mohammed Abdu Kaid: discussion and editing, K. Byrappa: supervision, investigation, and discussion.

Conflicts of interest

There are no conflicts to declare.

References

1 T. Zhang, Q. Tan, T. Zhang, J. Yang and S. Wang, A nexus approach engaging water rights transfer for addressing water scarcity in energy and food production under uncertainty, *J. Environ. Manage.*, 2022, **316**, 115163.
2 T. Zobeidi, J. Yaghoubi and M. Yazdanpanah, Developing a paradigm model for the analysis of farmers' adaptation to water scarcity, *Environ. Dev. Sustain.*, 2022, **1**, 1–26.
3 B. G. Maravilla Jr, N. M. Gan, D. Y. Guinanao, M. A. Pandan and K. J. Parohinog, Photocatalytic degradation of methyl orange in water using oyster shell-derived calcium oxide nanoparticles, *Bioresour. Technol. Rep.*, 2024, **13**, 101813.
4 H. Li, J. Yu, Y. Gong, N. Lin, Q. Yang, X. Zhang and Y. Wang, Perovskite catalysts with different dimensionalities for environmental and energy applications: a review, *Sep. Purif. Technol.*, 2022, **24**, 122716.
5 L. Huang, X. Huang, J. Yan, Y. Liu, H. Jiang, H. Zhang, J. Tang and Q. Liu, Research Progresses on the Application of Perovskite in Adsorption and Photocatalytic Removal of Water Pollutants, *J. Hazard. Mater.*, 2022, **19**, 130024.
6 M. R. Chetyrkina, L. Kameneva, D. V. Mishchenko, E. N. Klimanova, T. E. Sashenkova, U. Y. Allayarova, S. V. Kostyuk, L. A. Frolova, S. M. Aldoshin and P. A. Troshin, Lead, tin, bismuth or organics: assessment of potential environmental and human health hazards originating from mature perovskite PV technology, *Sol. Energy Mater. Sol. Cells*, 2023, **252**, 112177.
7 A. Khan, R. G. Bhoi, V. K. Saharan and S. George, Green calcium-based photocatalyst derived from waste marble powder for environmental sustainability: a review on synthesis and application in photocatalysis, *Environ. Sci. Pollut. Res.*, 2022, **11**, 1–29.
8 C. E. Torrence, C. S. Libby, W. Nie and J. S. Stein, Environmental and health risks of perovskite solar modules: case for better test standards and risk mitigation solutions, *iScience*, 2022, **15**, 105807.
9 Z. Du, C. Liu, J. Zhai, X. Guo, Y. Xiong, W. Su and G. He, A review of hydrogen purification technologies for fuel cell vehicles, *Catalysts*, 2021, **11**(3), 393.
10 S. Dursun, S. N. Koyuncu, İ. C. Kaya, G. G. Kaya, V. Kalem and H. Akyildiz, Production of CuO-WO_3 hybrids and their dye removal capacity/performance from wastewater by adsorption/photocatalysis, *J. Water Proc. Eng.*, 2020, **36**, 101390.
11 C. Postigo, P. Emiliano, D. Barceló and F. Valero, Chemical characterization and relative toxicity assessment of disinfection byproduct mixtures in a large drinking water supply network, *J. Hazard Mater.*, 2018, **359**, 166–173.
12 W. Zhang, L. Wang, Y. Yang, P. Gaskin and K. S. Teng, Recent advances on electrochemical sensors for the detection of organic disinfection byproducts in water, *ACS Sens.*, 2019, **4**(5), 1138–1150.
13 W. S. Koe, J. W. Lee, W. C. Chong, Y. L. Pang and L. C. Sim, An overview of photocatalytic degradation: photocatalysts, mechanisms, and development of photocatalytic membrane, *Environ. Sci. Pollut. Res.*, 2020, **27**(3), 2522–2565.
14 D. Chen, Y. Cheng, N. Zhou, P. Chen, Y. Wang, K. Li, S. Huo, P. Cheng, P. Peng, R. Zhang and L. Wang, Photocatalytic degradation of organic pollutants using TiO2-based photocatalysts: a review, *J. Cleaner Prod.*, 2020, **268**, 121725.
15 I. Nabi, Y. Chen, Z. Li, A. Iqbal, W. Liu, M. N. Afridi, A. Arifeen, W. Jin and L. Yang, Environmental application of perovskite material for organic pollutant-enriched wastewater treatment, *Coord. Chem. Rev.*, 2023, **495**, 215378.

16 A. Mills and S. Le Hunte, An overview of semiconductor photocatalysis, *J. Photochem. Photobiol., A*, 1997, **108**(1), 1–35.
17 D. S. Bhatkhande, V. G. Pangarkar and A. A. Beenackers, Photocatalytic degradation for environmental applications–a review, *J. Chem. Technol. Biotechnol.*, 2002, **77**(1), 102–116.
18 J. Luo, W. Zhang, H. Yang, Q. Fan, F. Xiong, S. Liu, D. S. Li and B. Liu, Halide perovskite composites for photocatalysis: a mini review, *EcoMat*, 2021, **3**(1), e12079.
19 Z. J. Bai, Y. Mao, B. H. Wang, L. Chen, S. Tian, B. Hu, Y. J. Li, C. T. Au and S. F. Yin, Tuning photocatalytic performance of $Cs_3Bi_2Br_9$ perovskite by g-C_3N_4 for C (sp_3)—H bond activation, *Nano Res.*, 2022, **12**, 1–9.
20 M. Masri, K. B. Girisha, A. Hezam, T. F. Qahtan, K. Alkanad, F. Masri, K. Namratha and K. Byrappa, Enhanced photocatalytic activity and stability of 2D $Cs_3Bi_2Br_9$ perovskite nanosheets synthesized via modified antisolvent method, *Colloids and Surfaces C: Environmental Aspects*, 2024, **2**, 100024.
21 P. Kanhere and Z. Chen, A review on visible light active perovskite-based photocatalysts, *Molecules*, 2014, **19**(12), 19995–20022.
22 C. G. Bischak, A. B. Wong, E. Lin, D. T. Limmer, P. Yang and N. S. Ginsberg, Tunable polaron distortions control the extent of halide demixing in lead halide perovskites, *J. Phys. Chem. Lett.*, 2018, **9**(14), 3998–4005.
23 T. A. Otitoju, P. U. Okoye, G. Chen, Y. Li, M. O. Okoye and S. Li, Advanced ceramic components: materials, fabrication, and applications, *J. Ind. Eng. Chem.*, 2020, **85**, 34–65.
24 M. Masri, A. Hezam, K. Alkanad, K. Prashantha, S. Manjunath, F. Masri, T. F. Qahtan and K. Byrappa, Metal Halide Perovskite-Based Photocatalysts for Organic Pollutants Degradation: Advances, Challenges, and Future Directions, *Colloids Surf., A*, 2024, **6**, 133387.
25 A. K. Jena, A. Kulkarni and T. Miyasaka, Halide perovskite photovoltaics: background, status, and future prospects, *Chem. Rev.*, 2019, **119**(5), 3036–3103.
26 X. Qian, Z. Chen, X. Yang, W. Zhao, C. Liu, T. Sun, D. Zhou, Q. Yang, G. Wei and M. Fan, Perovskite cesium lead bromide quantum dots: a new efficient photocatalyst for degrading antibiotic residues in organic system, *J. Cleaner Prod.*, 2020, **249**, 119335.
27 S. Bhattacharjee, S. P. Chaudhary and S. Bhattacharyya, Lead-free metal halide perovskite nanocrystals for photocatalysis in water, *ChemRxiv*, 2019, DOI: **10.26434/chemrxiv.9794270.v1**.
28 B. Yang, J. Chen, F. Hong, X. Mao, K. Zheng, S. Yang, Y. Li, T. Pullerits, W. Deng and K. Han, Lead-free, air-stable all-inorganic cesium bismuth halide perovskite nanocrystals, *Angew. Chem., Int. Ed.*, 2017, **56**(41), 12471–12475.
29 M. Leng, Y. Yang, K. Zeng, Z. Chen, Z. Tan, S. Li, J. Li, B. Xu, D. Li, M. P. Hautzinger and Y. Fu, All-inorganic bismuth-based perovskite quantum dots with bright blue photoluminescence and excellent stability, *Adv. Funct. Mater.*, 2018, **28**(1), 1704446.
30 R. Nelson, K. Santra, Y. Wang, A. Hadi, J. Petrich and M. Panthani, Synthesis and Optical Properties of Ordered-Vacancy Perovskite Cesium Bismuth Halide Nanocrystals, *Chem. Commun.*, 2018, **54**, 3640–3643.
31 M. K. Kim, J. Cha, H. Jin and M. Kim, Facile synthesis of $Cs_3Bi_2Br_9$ perovskite nanoplates with low-polarity antisolvents for photodetection applications, *Mater. Lett.*, 2023, **333**, 133577.
32 B. M. Bresolin, C. Günnemann, D. W. Bahnemann and M. Sillanpää, Pb-Free $Cs_3Bi_2I_9$ perovskite as a visible-light-active photocatalyst for organic pollutant degradation, *Nanomaterials*, 2020, **10**(4), 763.
33 A. G. Aragon, T. E. Wiggins, X. Ma and S. M. Geyer, Lead-free $Cs_3Bi_2Br_9$ and Cs_3Bi_2-xSbxBr_9 nanocrystals as photocatalysts with enhanced activity for the degradation of rhodamine in aqueous environments, *J. Photochem. Photobiol., A*, 2023, **436**, 114391.
34 J. N. Coleman, M. Lotya, A. O'Neill, S. D. Bergin, P. J. King, U. Khan, K. Young, A. S. d. Gaucher, R. J. Smith, I. V. Shvets, S. K. Arora, G. Stanton, H. Y. Kim, K. Lee, G. T. Kim, G. S. Duesberg, T. Hallam, J. J. Boland, J. J. Wang, J. F. Donegan, J. C. Grunlan, G. Moriarty, A. Shmeliov, R. J. Nicholls, J. M. Perkins, E. M. Grieveson, K. Theuwissen, D. W. McComb, P. D. Nellist and V. Nicolosi, *Science*, 2011, **331**(6017), 568–571.
35 B. Günay, H. Döğer, Z. F. Karagonlar and Ö. Sağlam, Ag-intercalation of Tm^{3+}/Er^{3+} Co-doped layered perovskites and their exfoliated 2D nanosheets with an enhanced antibiofilm and antibacterial activity, *Mater. Today Commun.*, 2022, **33**, 104972.
36 D. Jiang, T. Wang, Q. Xu, D. Li, S. Meng and M. Chen, Perovskite oxide ultrathin nanosheets/g-C_3N_4 2D-2D heterojunction photocatalysts with significantly enhanced photocatalytic activity towards the photodegradation of tetracycline, *Appl. Catal., B*, 2017, **201**, 617–628.
37 J. Chen, Y. Shi, Y. He and T. Zhai, Two-dimensional Ruddlesden-Popper perovskite nanosheets: synthesis, optoelectronic properties and miniaturized optoelectronic devices, *FlatChem*, 2019, **17**, 100116.
38 A. P. Kumar, D. Bilehal, T. Desalegn, S. Kumar, F. Ahmed, H. A. Murthy, D. Kumar, G. Gupta, D. K. Chellappan, S. K. Singh and K. Dua, Studies on synthesis and characterization of Fe_3O_4@ SiO_2@ Ru hybrid magnetic composites for reusable photocatalytic application, *Adsorpt. Sci. Technol.*, 2022, **2022**, 1–8.
39 B. Abebe and H. C. Ananda Murthy, Synthesis and characterization of Ti-Fe oxide nanomaterials for lead removal, *J. Nanomater.*, 2018, **2018**, 1.
40 B. Abebe, E. A. Zereffa and H. A. Murthy, Synthesis of poly (vinyl alcohol)-aided ZnO/Mn_2O_3 nanocomposites for acid orange-8 dye degradation: mechanism and antibacterial activity, *ACS Omega*, 2020, **6**(1), 954–964.
41 B. Abebe, H. A. Murthy, E. A. Zereffa and Y. Qiang, Synthesis and characterization of PVA-assisted metal oxide nanomaterials: surface area, porosity, and electrochemical property improvement, *J. Nanomater.*, 2020, **2020**, 1–4.

42 B. Abebe, C. R. Ravikumar, E. A. Zereffa, A. N. Kumar and H. A. Murthy, Photocatalytic and superior ascorbic acid sensor activities of PVA/Zn-Fe-Mn ternary oxide nanocomposite, *Inorg. Chem. Commun.*, 2021, **123**, 108343.
43 G. Viruthagiri, P. Kannan and V. K. Indhumathi, Photocatalytic activity of α-phase bismuth oxide nanoparticles under visible light, *Int. J. Adv. Sci. Res.*, 2017, **2**, 1–7.
44 B. Abebe, E. A. Zereffa, H. A. Murthy and C. R. Ravikumar, A novel poly (vinyl alcohol)-aided ZnO/Fe_2O_3 nanocomposite as an ascorbic acid sensor, *J. Mater. Sci.: Mater. Electron.*, 2021, **32**(6), 7778–7790.
45 M. A. Kumar, B. Abebe, H. P. Nagaswarupa, H. A. Murthy, C. R. Ravikumar and F. K. Sabir, Enhanced photocatalytic and electrochemical performance of TiO_2-Fe_2O_3 nanocomposite: its applications in dye decolorization and as supercapacitors, *Sci. Rep.*, 2020, **10**(1), 1249.
46 L. Leontie, M. Caraman, M. Delibaș and G. I. Rusu, Optical properties of bismuth trioxide thin films, *Mater. Res. Bull.*, 2001, **36**(9), 1629–1637.
47 T. R. Das, S. Patra, R. Madhuri and P. K. Sharma, Bismuth oxide decorated graphene oxide nanocomposites synthesized via sonochemical assisted hydrothermal method for adsorption of cationic organic dyes, *J. Colloid Interface Sci.*, 2018, **509**, 82–93.
48 Z. Hamid, Synthesis of bismuth oxide nano powders via electrolysis method and study the effect of change voltage on the size for it, *Aust. J. Basic Appl. Sci.*, 2017, **11**(7), 97–101.
49 A. K. Chakraborty, S. A. Razzaque, M. A. Haque, A. Akter, S. Ganguli, M. N. Islam, A. S. Nur and M. A. Sabur, Fabrication of visible-light induced fluorine doped bismuth oxide ($Bi_2O_{3-X}F_X$) photocatalyst in degrading textile dyes from wastewater, *Chemistry of Inorganic Materials*, 2023, **1**, 100019.
50 M. K. Kim, J. Cha, H. Jin and M. Kim, Facile synthesis of $Cs_3Bi_2Br_9$ perovskite nanoplates with low-polarity antisolvents for photodetection applications, *Mater. Lett.*, 2023, **333**, 133577.
51 A. Hezam, K. Namratha, Q. A. Drmosh, Z. H. Yamani and K. J. Byrappa, Synthesis of heterostructured Bi_2O_3–CeO_2–ZnO photocatalyst with enhanced sunlight photocatalytic activity, *Ceram. Int.*, 2017, **43**(6), 5292–5301.
52 F. Lazarini, Caesium enneabromodibismuthate (III), *Acta Crystallogr. Sect. B Struct. Crystallogr. Cryst. Chem.*, 1977, **33**(9), 2961–2964.
53 S. C. Myneni, S. J. Traina, G. A. Waychunas and T. J. Logan, Vibrational spectroscopy of functional group chemistry and arsenate coordination in ettringite, *Geochim. Cosmochim. Acta*, 1998, **62**(21–22), 3499–3514.
54 S. G. Ullattil, P. Periyat, B. Naufal and M. A. Lazar, Self-Doped ZnO Microrods High Temperature Stable Oxygen Deficient Platforms for Solar Photocatalysis, *Ind. Eng. Chem. Res.*, 2016, **55**(22), 6413–6421.
55 M. Faisal, S. B. Khan, M. M. Rahman, A. Jamal, K. Akhtar and M. M. Abdullah, Role of ZnO-CeO_2 nanostructures as a photocatalyst and chemi-sensor, *J. Mater. Sci. Technol.*, 2011, **27**(7), 594–600.
56 K. Gurunathan, Photocatalytic hydrogen production using transition metal ions-doped γ-Bi_2O_3 semiconductor particles, *Int. J. Hydrogen Energy*, 2004, **29**(9), 933–940.
57 D. S. Kim and S. Y. Kwak, The hydrothermal synthesis of mesoporous TiO_2 with high crystallinity, thermal stability, large surface area, and enhanced photocatalytic activity, *Appl. Catal., A*, 2007, **323**, 110–118.
58 G. Li, H. Jang, S. Liu, Z. Li, M. G. Kim, Q. Qin, X. Liu and J. Cho, The synergistic effect of Hf-O-Ru bonds and oxygen vacancies in Ru/HfO_2 for enhanced hydrogen evolution, *Nat. Commun.*, 2022, **13**(1), 1270.
59 J. Chastain and R. C. King Jr, *Handbook of X-Ray Photoelectron Spectroscopy*, Perkin-Elmer Corporation, 1992, vol. 40, p. 221.
60 K. Alkanad, A. Hezam, Q. A. Drmosh, S. S. Ganganakatte Chandrashekar, A. A. AlObaid, I. Warad, M. A. Bajiri and L. Neratur Krishnappagowda, Construction of Bi2S3/TiO2/MoS2 S-scheme heterostructure with a switchable charge migration pathway for selective CO2 reduction, *Sol. RRL*, 2021, **5**(11), 2100501.
61 J. Ma, L. Xu, Z. Yin, Z. Li, X. Dong, Z. Song, D. Chen, R. Hu, Q. Wang, J. Han and Z. Yang, "One stone four birds" design atom co-sharing BiOBr/Bi_2S_3 S-scheme heterojunction photothermal synergistic enhanced full-spectrum photocatalytic activity, *Appl. Catal., B*, 2024, **344**, 123601.
62 Y. Li, T. Liu, Z. Cheng, Y. Peng, S. Yang and Y. Zhang, Facile synthesis of high crystallinity and oxygen vacancies rich bismuth oxybromide upconversion nanosheets by air-annealing for UV–Vis–NIR broad spectrum driven bisphenol A degradation, *Chem. Eng. J.*, 2021, **421**, 127868.
63 Y. Wu, W. Xu, W. Tang, Z. Wang, Y. Wang, Z. Lv, Y. Zhang, W. Zhong, H. L. Cai, R. Yang and X. S. Wu, In-situ annealed "M-scheme" MXene-based photocatalyst for enhanced photoelectric performance and highly selective CO_2 photoreduction, *Nano Energy*, 2021, **90**, 106532.
64 X. Lian, J. Zhang, Y. Zhan, Y. Zhang, S. Yang, Z. Chen, Y. Dong, W. Fang and X. Yi, Engineering $BiVO_4$@ Bi_2S_3 heterojunction by cosharing bismuth atoms toward boosted photocatalytic Cr (VI) reduction, *J. Hazard. Mater.*, 2021, **406**, 124705.
65 A. B. Murphy, Bandgap determination from diffuse reflectance measurements of semiconductor films, and application to photoelectrochemical water-splitting, *Sol. Energy Mater. Sol. Cells*, 2007, **91**(14), 1326–1337.
66 M. Chireh and M. Naseri, Effect of calcination temperature on the physical properties of $LiFe_5O_8$ nanostructures, *Adv. Powder Technol.*, 2019, **30**(5), 952–960.
67 M. A. Kumar, H. P. Nagaswarupa, C. R. Ravikumar, S. C. Prashantha, H. Nagabhushana and A. S. Bhatt, Green engineered nano MgO and ZnO doped with Sm^{3+}: synthesis and a comparison study on their characterization, PC activity and electrochemical properties, *J. Phys. Chem. Solids*, 2019, **127**, 127–139.
68 P. Rekha, R. Muhammad and P. Mohanty, Sonochemical synthesis of cyclophosphazene bridged mesoporous organosilicas and their application in methyl orange,

congo red and Cr (VI) removal, *RSC Adv.*, 2015, **5**(83), 67690–67699.

69 M. A. Rauf, M. A. Meetani, A. Khaleel and A. Ahmed, Photocatalytic degradation of methylene blue using a mixed catalyst and product analysis by LC/MS, *Chem. Eng. J.*, 2010, **157**, 373–378.

70 S. Zhou, Z. Du, X. Li, Y. Zhang, Y. He and Y. Zhang, Degradation of methylene blue by natural manganese oxides: kinetics and transformation products, *R. Soc. Open Sci.*, 2019, **6**(1–12), 190351.

71 M. S. Xaba, J.-H. Noh and R. Meijboom, Catalytic activity of different sizes of Ptn/Co_3O_4 in the oxidative degradation of Methylene Blue with H_2O_2, *Appl. Surf. Sci.*, 2019, **467–468**, 868–880.

72 R. Rameshbabu, R. Vinoth, M. Navaneethan, Y. Hayakawa and B. Neppolian, Fabrication of Cu_2MoS_4 hollow nanotubes with rGO sheets for enhanced visible light photocatalytic performance, *CrystEngComm*, 2017, **19**, 2475–2486.

73 M. Zare, K. Namratha, M. S. Thakur, S. Yallappa and K. Byrappa, Comprehensive biological assessment and photocatalytic activity of surfactant assisted solvothermal synthesis of ZnO nanogranules, *Mater. Chem. Phys.*, 2018, **215**, 148–156.

74 Y. R. Girish, G. Alnaggar, A. Hezam, M. B. Nayan, G. Nagaraju and K. Byrappa, Facile and rapid synthesis of solar-driven TiO_2/g-C_3N_4 heterostructure photocatalysts for enhanced photocatalytic activity, *J. Sci.:Adv. Mater. Devices*, 2022, **7**(2), 100419.

75 Q. A. Drmosh, A. Hezam, A. H. Hendi, M. Qamar, Z. H. Yamani and K. Byrappa, Ternary Bi_2S_3/MoS_2/TiO_2 with double Z-scheme configuration as high performance photocatalyst, *Appl. Surf. Sci.*, 2020, **499**, 143938.

76 R. Cai, J. G. Wu, L. Sun, Y. J. Liu, T. Fang, S. Zhu, S. Y. Li, Y. Wang, L. F. Guo, C. E. Zhao and A. Wei, 3D graphene/ZnO composite with enhanced photocatalytic activity, *Mater. Des.*, 2016, **90**, 839–844.

77 X. Cui, Y. Wang, G. Jiang, Z. Zhao, C. Xu, A. Duan, J. Liu, Y. Wei and W. Bai, The encapsulation of CdS in carbon nanotubes for stable and efficient photocatalysis, *J. Mater. Chem. A*, 2014, **2**(48), 20939–20946.

78 D. Xu, S. Cao, J. Zhang, B. Cheng and J. Yu, Effects of the preparation method on the structure and the visible-light photocatalytic activity of Ag_2CrO_4, *Beilstein J. Nanotechnol.*, 2014, **5**(1), 658–666.

79 Y. Baghdadi, F. Temerov, J. Cui, M. Daboczi, E. Rattner, M. S. Sena, I. Itskou and S. Eslava, $Cs_3Bi_2Br_9$/g-C_3N_4 Direct Z-Scheme Heterojunction for Enhanced Photocatalytic Reduction of CO_2 to CO, *Chem. Mater.*, 2023, **35**(20), 8607–8620.

80 C. Wang, Y. Zhao, C. Cheng, Q. Li, C. Guo and Y. Hu, S-scheme heterojunction photocatalysts: mechanism, challenges and opportunities, *Coord. Chem. Rev.*, 2024, **521**, 216177.

81 F. Li, G. Zhu, J. Jiang, L. Yang, F. Deng and X. Li, A review of updated S-scheme heterojunction photocatalysts, *J. Mater. Sci. Technol.*, 2024, **177**, 142–180.

82 B. Zhu, J. Sun, Y. Zhao, L. Zhang and J. Yu, Construction of 2D S-scheme heterojunction photocatalyst, *Adv. Mater.*, 2024, **36**(8), 2310600.

83 Q. Xu, L. Zhang, B. Cheng, J. Fan and J. Yu, S-scheme heterojunction photocatalyst, *Chem*, 2020, **6**(7), 1543–1559.

84 A. H. Bashal, K. Alkanad, M. Al-Ghorbani, S. B. Aoun and M. A. Bajiri, Synergistic effect of cocatalyst and S-scheme heterojunction over 2D/2D g-C_3N_4/MoS_2 heterostructure coupled Cu nanoparticles for selective photocatalytic CO_2 reduction to CO under visible light irradiation, *J. Environ. Chem. Eng.*, 2023, **11**(2), 109545.

85 H. Yang, G. Liu, X. Liu, X. Wang, D. Wang, Y. Huang, J. Zhang, Z. Yang, W. Yang, M. Wu and L. Zhao, *Ultrasound-Assisted Synthesis of Ag/Agvo$_3$ Nanocomposites for Enhanced Photocatalytic Reduction of Cr (Vi) Under Visible Light*, 2024, DOI: **10.2139/ssrn.4985700**.

86 J. Wang, B. Wang, W. Zhang, Y. Xiao, H. Xu, Y. Liu, Z. Liu, J. Zhang and Y. Jiang, Visible-light-driven double-shell $SnIn_4S_8$/TiO_2 heterostructure with enhanced photocatalytic activity for MO removal and Cr (VI) cleanup, *Appl. Surf. Sci.*, 2022, **587**, 152867.

87 L. Xin, L. Yu, Y. Liu, Y. Zhang, H. Zhu, L. A. Rodrigues and D. A. Reddy, *Halogen Atoms Doped Feocl Promoting Fe (II)/Fe (III) Cycles to Accelerate the Photo-Fenton-Like Progress*, 2024, DOI: **10.2139/ssrn.4952100**.

88 Q. Sun, W. Ye, J. Wei, L. Li, J. Wang, J. H. He and J. M. Lu, Lead-free perovskite $Cs_3Bi_2Br_9$ heterojunctions for highly efficient and selective photocatalysis under mild conditions, *J. Alloys Compd.*, 2022, **893**, 162326.